ACADEMIC PRESS

Available online at www.sciencedirect.com

SCIENCE DIRECT®

Journal of Computational Physics 186 (2003) 545–581

JOURNAL OF COMPUTATIONAL PHYSICS

www.elsevier.com/locate/jcp

An Eulerian gyrokinetic-Maxwell solver

J. Candy *, R.E. Waltz

General Atomics, P.O. Box 85608, San Diego, CA, USA

Received 30 April 2002; received in revised form 15 October 2002; accepted 5 February 2003

Abstract

In this report we present a time-explicit, Eulerian numerical scheme for the solution of the nonlinear gyrokinetic-Maxwell equations. The treatment of electrons is fully drift-kinetic, transverse electromagnetic fluctuations are included, and profile variation is allowed over an arbitrary radial annulus. The code, `gyro`, is benchmarked against analytic theory, linear eigenmode codes, and nonlinear electrostatic gyrokinetic particle-in-cell codes. We have attempted preliminary finite-β calculations in the range $\beta/\beta_{\text{crit}} = [0.0, 0.5]$ for a reference discharge. Detailed diagnostic data is presented for these simulations, along with a number of caveats which reflect the uncharted nature of the parameter regime.

PACS: 52.55.Dy; 52.30.Gz; 52.35.Qz; 52.35.Ra; 52.65.Tt

Keywords: Turbulence; Gyrokinetic; Eulerian

1. Introduction

The most aggressively studied and developed concept for power production by fusion reactions is the tokamak. Nevertheless, despite continuous advances in understanding the behavior of tokamak plasmas, uncertainties remain in predicting the confinement properties and performance of successively larger, reactor-scale devices. Specifically, while present tokamak experiments can provide discharges with dimensionless parameters characteristic of a reactor – such as β, safety factor, elongation, aspect ratio, etc. – they cannot simultaneously achieve the small expected values of ρ_*. With regard to a theoretical approach, it is believed that the coupled gyrokinetic-Maxwell (GKM) equations lay a firm foundation for the first-principles calculation of anomalous tokamak transport. Consequently, the numerical solution of the nonlinear GKM equations including both electromagnetic fluctuations and radial profile variation has for years been a computational physics "Grand Challenge". Complicated geometry, particle trapping, multiple space and time-scales, and tiny electron-to-ion mass ratio preclude the use of "textbook" numerical approaches.

* Corresponding author.
E-mail address: jeff.candy@gat.com (J. Candy).

0021-9991/03/$ - see front matter
doi:10.1016/S0021-9991(03)00079-2

The understanding and study of tokamak microinstabilities has, for many years now, been shaped by extensive use of existing radially local, numerical linear solvers. The most comprehensive of these are the eigenvalue code by Rewoldt et al. (`full`) [1], and the initial-value code by Kotschenreuther et al. (`gks`) [2]. Both include kinetic electron dynamics, electromagnetic effects, and particle trapping – and both use Eulerian (also referred to as "continuum") numerical algorithms. Efficiency in `gks` and `full` is achieved through the use of periodic, or "flux-tube", radial boundary conditions, whereby both operate at vanishingly small ρ_*, with $\rho_* = \rho_i/a$ the ratio of the ion gyroradius to plasma minor radius.

With regard to the flux-tube approximation, in the vanishing-ρ_* limit (when the turbulence scale-length is proportional to ρ_s), random-walk arguments applied to the GKM equations predict ion thermal diffusivities, χ_i, with a natural *gyroBohm scaling*: $\chi_i \sim \rho_s \times \rho_s \times (c_s/a)$. Here, $c_s \doteq \sqrt{T_e/m_i}$ is the sound speed, $\rho_s \doteq c_s/\Omega_{ci}$ is the ion sound Larmor radius, and Ω_{ci} is the ion cyclotron frequency. However, present-day tokamaks often produce results closer to *Bohm scaling*, $\chi_i \sim \rho_s \times a \times (c_s/a)$, to be expected when the turbulence scale-length involves the system size a. Since tokamaks operate at finite ρ_*, it is perhaps unsurprising that explanations based on finite-ρ_* effects (basically, profile variation) have been put forward [3,4] to explain the breaking of gyroBohm scaling.

Algorithms based on solving for a few moments of the nonlinear GKM equations ("gyrofluid" algorithms) led to the discovery of the importance of zonal flows [5–7], to the quantitative identification of the linear ion temperature grad (ITG) threshold and consequent "stiffness" as crucial issues for understanding experimental data and predicting performance [2,8,9], and to the first studies of interacting ITG and TEM turbulence [10–12]. The first efforts to solve the nonlinear toroidal gyrokinetic equations directly were of the gyrokinetic particle-in-cell (GK-PIC) type [13–16] due to the relative algorithmic compactness and subsequent ease of coding in comparison with the Eulerian solvers which followed [17,18]. Gyrofluid, GK-PIC and Eulerian GK efforts proved to be successful for the study of ITG mode transport with adiabatic electrons (ITG-ae), and unlocked the door to a deeper understanding of complex phenomena at work in tokamak plasmas.

Heretofore, nonlinear GK-PIC simulations have been limited to electrostatic fluctuations, and nonlinear Eulerian simulations have been limited to flux-tubes. Simulations realistic enough to understand the nongyroBohm scaling of many existing experiments, and to make credible extrapolations to reactor-scale devices, require both finite-β (electromagnetic) and finite-ρ_s (profile) effects. Here, β is the ratio of plasma pressure to magnetic pressure. Indeed, at the time of writing of this report, there is significant effort aimed at the inclusion of electromagnetic effects into existing GK-PIC codes. In connection with these efforts, a variety of promising approximate schemes have been proposed: "electromagnetic split-weight" [19], "fluid-kinetic hybrid electrons" [20], "zero electron inertia fluid electrons" [21], and "kinetic electron closure" [22,23]. The issue of electromagnetic effects on microturbulence-driven plasma transport has also recently been explored by Snyder and Hammett [24] using a gyrofluid model. This work suggests that a significant β-dependence of the thermal diffusivity is to be expected, with a strong increase in transport as β nears the ideal ballooning stability limit.

By the end of 2000, two nonlinear, toroidal, electromagnetic codes were in production use: the `gs2` code [17] (a nonlinear generalization of `gks`), and the `gene` code [18]. The latter, which neglects magnetic trapping but retains full parallel electron dynamics, was developed by Jenko for edge turbulence studies. Both `gs2` and `gene` are Eulerian flux-tube codes.

To address the problem of turbulence and transport in tokamaks at finite-β, we developed `gyro` – a parallel, Eulerian GKM code with gyrokinetic ions and electrons capable of treating finite-ρ_* electromagnetic microturbulence. `gyro` can operate in either (i) *flux-tube mode* with periodic radial boundary conditions and no profile variation, or (ii) *radial-slice mode* with nonperiodic boundary conditions and radial profile variation. In the latter mode, an adaptive source *must* be added to maintain the equilibrium profiles. Otherwise substantial changes in the equilibrium gradients can be nonlinearly generated, and correspondingly incorrect measures of the transport scaling will be produced. Although `gyro` has been

used to demonstrate the breaking of gyroBohm scaling by profile-shear stabilization in the electrostatic limit [25], we do not treat profile variation – and do not discuss the adaptive source technique – in the present work. Our purpose here is to document the numerical methods (and some hard-learned lessons) required for electromagnetic simulation, and where possible to benchmark `gyro` with other gyrokinetic codes.

2. Definitions

2.1. Notation

To avoid confusion, in this paper we use the bare symbol $\imath$ to denote the imaginary number $\sqrt{-1}$ and the dotted symbol i to denote the radial grid index. To distinguish species, we hereafter use the subscripts 1 (ions) and 2 (electrons). In a few cases, where no danger of ambiguity exists, we retain the more intuitive subscripts i and e.

2.2. Coordinates and geometry

`gyro` uses a toroidal coordinate system (r,θ,ζ) based on the Miller equilibrium model [26]. r is a flux-surface label, θ is an angle in the poloidal plane, and ζ is an angle in the toroidal direction. Physically, r is the mid-plane minor radius, such that $\hat{\mathbf{b}}\cdot\nabla r = 0$ with $\hat{\mathbf{b}}$ the unit vector directed along the unperturbed magnetic field. The toroidal coordinate ζ is defined in terms of the physical toroidal angle ζ^{p} as

$$\zeta \doteq \zeta^{\mathrm{p}} - \int_0^\theta \mathrm{d}\theta\,\hat{q}, \quad \text{where } \hat{q} \doteq \frac{\hat{\mathbf{b}}\cdot\nabla\zeta^{\mathrm{p}}}{\hat{\mathbf{b}}\cdot\nabla\theta} \tag{1}$$

is the local safety factor. By construction, ζ is constant along a field line: $\hat{\mathbf{b}}\cdot\nabla\zeta = 0$. We will repeatedly make use of the flux-surface-averaging operator, $\mathfrak{F}$, defined as

$$\mathfrak{F}[f] \doteq \frac{1}{\mathscr{J}_0}\int_{-\pi}^{\pi}\mathrm{d}\theta\,\mathscr{J}(r,\theta)f(\theta), \quad \text{where } \mathscr{J}_0 \doteq \int_{-\pi}^{\pi}\mathrm{d}\theta\,\mathscr{J}(r,\theta). \tag{2}$$

The quantity $\mathscr{J}$, related to the Jacobian determinant, is defined as

$$\mathscr{J} \doteq \frac{R(r,\theta)}{R_0(r)}\,\frac{1}{r|\nabla\theta|}\,\frac{1}{|\nabla r|}, \tag{3}$$

in terms of which we can define a shaping factor $g_\theta(r,\theta) = \mathscr{J}\hat{B}$. In Eq. (3), R is the horizontal distance from the toroidal symmetry axis to the point (r,θ) (the major radius), whereas R_0 is the distance from the toroidal symmetry axis to the center of the flux surface at r. In the absence of Shafranov shift, R_0 is constant and equal to the location of the magnetic axis. The normalized magnetic field strength is $\hat{B} = B/(g_r B_0)$, where B is the real field strength, B_0 is the on-axis field strength, and

$$g_r(r) \doteq \frac{\rho\,\mathrm{d}\rho}{r\,\mathrm{d}r}\Bigg/\left(\frac{\rho\,\mathrm{d}\rho}{r\,\mathrm{d}r}\right)_{r=r_*}. \tag{4}$$

The radius r_* is an arbitrary reference position, typically chosen to be the center of the radial domain. The quantity ρ is defined through the toroidal flux $\chi_{\mathrm{t}} \doteq B_0\rho^2/2$. Details are given in [27]. For circular $s-\alpha$ geometry, we have $g_\theta = g_r = 1$ and $1/\hat{B} = 1 + (r/R_0)\cos\theta$. With $q(r) = \mathfrak{F}[\hat{q}]$ the average safety factor, the parallel derivative in (r,θ,ζ)-coordinates can be written

$$\hat{\mathbf{b}}\cdot\nabla = (\hat{\mathbf{b}}\cdot\nabla\theta)\frac{\partial}{\partial\theta} = \frac{1}{g_\theta}\frac{1}{qR_0}\frac{\partial}{\partial\theta}. \tag{5}$$

2.3. Units and normalizations

Our choice of units is summarized in Table 1. Beyond this, we introduce normalized densities, $n_s(r)$, and normalized gyrocenter distributions, $f_s(r)$. In terms of these, the physical densities, temperatures and distributions are given by

$$n_s^{\mathrm{p}}(r) = n_s(r)n_{2*}, \quad T_s^{\mathrm{p}}(r) = T_s(r)T_{2*} \quad \text{and} \quad f_s^{\mathrm{p}}(r) = f_s(r)n_{2*}F_s^M. \tag{6}$$

The physical scalar and magnetic vector potentials are related to the normalized versions by

$$\phi(r) = \frac{e\phi^{\mathrm{p}}(r)}{T_{2*}} \quad \text{and} \quad A_\parallel(r) = \frac{c_s}{c}\frac{eA_\parallel^{\mathrm{p}}(r)}{T_{2*}}, \tag{7}$$

respectively. The index s denotes the species, electron or ion, and the superscript p denotes a *physical* quantity. n_{2*} and T_{2*} are the physical electron density and temperature at the reference position r_*. Above, $F_s^M \doteq e^{-W/T_s}/(\pi^{3/2}v_s^3)$ and $T_s(r) = m_s v_s^2/2$. The equilibrium distribution is $F_0 s = n_s F_s^M$, and $W \doteq m(v_\parallel^2 + v_\perp^2)/2$ is the unperturbed energy. By making these specifications, we preclude the study of, for example, strongly rotating plasmas. While the algorithms we describe in this report are compatible with the inclusion of equilibrium rotation, we defer a discussion of such a generalizations to future work.

Two important parameters which appear throughout this report are the reference *ion-sound gyroradius* and reference *electron beta*, defined as

$$\rho_s \doteq \frac{c_s}{eB_0/m_1 c} \quad \text{and} \quad \beta_e \doteq \frac{n_{2*}T_{2*}}{B_0^2/8\pi}. \tag{8}$$

2.4. The velocity-space integration operator

For each species we introduce the velocity-integration operator $V[\cdot]$

$$\int \mathrm{d}^3 v F^M f(\mathbf{X}_g, v_\perp, v_\parallel; t) = V[f], \tag{9}$$

where $\mathbf{X}_g$ is the fixed gyrocenter location. Explicitly, we have

$$V[f] \doteq \sum_\sigma \frac{1}{2\sqrt{\pi}}\int_0^\infty \mathrm{d}\epsilon\, \mathrm{e}^{-\epsilon}\sqrt{\epsilon}\int_0^1 \frac{\mathrm{d}(\lambda\hat{B})}{\sqrt{1-\lambda\hat{B}}} f(r,\theta,\zeta;\epsilon,\lambda,\sigma;t), \tag{10}$$

Table 1
Summary of units used in `gyro`

Dimension	Unit	Description
Length	a	Midplane minor radius at separatrix
Velocity	c_s	Sound speed ($\sqrt{T_{2*}/m_1}$)
Mass	m_1	Ion mass
Time	a/c_s	
Temperature	T_{2*}	Electron temperature

where for brevity, species subscripts have been omitted. The normalized integration variables are $\epsilon \doteq W/T$, $\lambda \doteq v_\perp^2/(\hat{B}v^2)$ and $\sigma = \mathrm{sgn}(v_\parallel)$. It can be verified that $V[1] = 1$. In writing Eq. (10), we explicitly rule out consideration of nonMaxwellian particle distributions. The generalization to a fast ion population is beyond the scope of the present work.

2.5. Representation of perturbed quantities

We expand the perturbed quantities $(\phi, A_\parallel, f)$ as Fourier series in ζ. For example, the potential is written as

$$\phi = \sum_n \phi_n(r,\theta)\, \mathrm{e}^{-\imath n\zeta}. \tag{11}$$

Although the physical field, ϕ, is 2π-periodic in θ, this representation has the implication that the Fourier coefficients, ϕ_n, are nonperiodic, and satisfy the phase condition $\phi_n(r,\pi) = \mathscr{P}\phi_n(r,-\pi)$, where

$$\mathscr{P}(n,r) \doteq \mathrm{e}^{-2\pi\imath n q(r)}. \tag{12}$$

Since ϕ is real, the coefficients satisfy $\phi_n^* = \phi_{-n}$.

3. Simulation equations

Derivations of the nonlinear GKM equations appear in numerous other publications [28,29], so we refer the reader to the recent paper by Jenko et al. [30] (and references therein) as a starting point. In the sections that follow, we cast these equations in forms directly amenable to numerical solution.

3.1. The gyrokinetic equation

Rather than the real gyro-center distribution, f_{sn}, we prefer to work with a function, h_{sn}, chosen in order to eliminate the time derivative of $A_\parallel$ from the GK equation. The relation between f_{sn} and h_{sn} is $h_{sn} \doteq f_{sn} + z_\mathrm{s}\alpha_\mathrm{s} v_{\parallel\mathrm{s}}(\mathscr{G}A_\parallel)_n$, where z_s is the species charge, and $\alpha_\mathrm{s} \doteq n_\mathrm{s}/T_\mathrm{s}$. $\mathscr{G}$, the gyroaveraging operator, will be described in detail in Section 7. By h_{sn}, we mean the nth toroidal harmonic of h_s, or $(h_\mathrm{s})_n$. In terms of h_{sn}, the gyrokinetic equation, including collisions, is

$$\frac{\partial h_{sn}}{\partial t} - \mathscr{C}[h_{sn} - z_\mathrm{s}\alpha_\mathrm{s} v_\parallel (\mathscr{G}A_\parallel)_n] = \mathrm{RHS}_n(r,\theta;\lambda,\epsilon), \tag{13}$$

$$\mathrm{RHS}_n = \left[-\frac{1}{R_0 q}\frac{v_{\parallel\mathrm{s}}(r,\theta)}{g_\theta(r,\theta)}\frac{\partial}{\partial\theta} + \imath\omega_{\mathrm{ds}}^{(1)} + \imath\omega_{\mathrm{ds}}^{(r)}\frac{\partial}{\partial r}\right](h_{sn} + z_\mathrm{s}\alpha_\mathrm{s}(\mathscr{G}u_\mathrm{s})_n) - \imath n_\mathrm{s}\omega_{*\mathrm{s}}(\mathscr{G}u_\mathrm{s})_n + \imath\hat{\rho}\{\mathscr{G}u_\mathrm{s}, h\}_n, \tag{14}$$

where $u_\mathrm{s} \doteq \phi - v_{\parallel\mathrm{s}}A_\parallel$,

$$v_{\parallel\mathrm{s}}(r,\theta) \doteq \sigma\sqrt{\frac{m_1}{m_\mathrm{s}}}\sqrt{2\epsilon T_\mathrm{s}(r)(1-\lambda\hat{B}(r,\theta))}. \tag{15}$$

The bracket $\{\cdot,\cdot\}$ which describes the nonlinear $\mathbf{E}\times\mathbf{B}$ and magnetic flutter dynamics, is defined and discussed in Section 8. The coefficient of the bracket is $\hat{\rho} \doteq (q/rg_r)\rho_\mathrm{s}$. The curvature drift coefficients, $\omega_d^{(1)}$ and $\omega_d^{(r)}$, as well as the diamagnetic frequency ω_*, are given by

$$\omega_{*\mathrm{s}} \doteq \frac{k_\theta\rho_\mathrm{s}}{g_r}\left[\frac{a}{L_{n\mathrm{s}}} + (\epsilon - 3/2)\frac{a}{L_{T\mathrm{s}}}\right], \tag{16}$$

$$\omega_{\rm ds}^{(1)} \doteq k_\theta \rho_{\rm s} \frac{g_q}{\hat{B}} \frac{2z_{\rm s}T_{\rm s}}{R_0} \epsilon \left(1 - \frac{\lambda \hat{B}}{2}\right) \left\{ [[\cos]](r,\theta) + [[k_x/k_y]][[\sin]](r,\theta) \right\}, \tag{17}$$

$$\omega_{\rm ds}^{(r)} \doteq -i\rho_{\rm s} \frac{|\nabla r|}{\hat{B}} \frac{2z_{\rm s}T_{\rm s}}{R_0} \epsilon \left(1 - \frac{\lambda \hat{B}}{2}\right) [[\sin]](r,\theta). \tag{18}$$

Above, $k_\theta \doteq nq/r$ and $g_q \doteq (1/q)(rB/RB_p)$. Definitions of the other geometry-dependent factors [[cos]], [[sin]] and $[[k_x/k_y]]$ appear in [27]. In the limit of circular $s-\alpha$ geometry, we have $g_r, g_q, |\nabla r| \to 1$, [[cos]] $\to$ cos, [[sin]] $\to$ sin and $[[k_x/k_y]] \to s\theta - \alpha_{\rm MHD} \sin\theta$. Although the simulations performed in this report use constant shear and monotonic q-profiles, all discretization schemes are perfectly suitable (and have indeed been tested) for nonmonotonic q variation.

Further, in the present work, we are not interested in fluctuations at very-short (ETG-scale) wavelengths, and hereafter set $\mathcal{G} \to 1$ for electrons. This yields computational savings, especially for the sparse Ampère solver of Section 5. The approach used to solve Eq. (13) numerically can be briefly summarized: first, we discretize the spatial operators contained in RHS, and then apply an explicit time-integration algorithm to the resulting ordinary differential equations. This technique is referred to as the *method of lines* (MOL).

3.2. The Poisson equation

When the full kinetic electron response is included, the Poisson equation [30] is

$$\alpha_1(1 - \mathcal{R})\phi_n = V_1[\mathcal{G}h_{1n}] - V_2[h_{2n}], \tag{19}$$

where $\mathcal{R} = V_1[\mathcal{G}\mathcal{G}]$ is a velocity-space-integrated double gyroaverage. The appearance of the gyro-operators in Eq. (19) is a consequence of the mapping from physical to gyro-center coordinates in the integrand [29]. The discrete form of $\mathcal{R}$ is discussed in Section 7. We remind the reader that the subscript 1 denotes *ions* while 2 denotes *electrons*. For simulation of electrostatic ITG, the physical complexity of the dynamics is greatly reduced if the electron distribution is replaced by the *adiabatic* response

$$h_{2n} \to \alpha_2(\phi_n - \delta_{n0}\mathfrak{F}[\phi_0]), \tag{20}$$

where δ_{n0} is the Kronecker delta function. The Poisson equation for the adiabatic electron model is then

$$\alpha_1(1 - \mathcal{R})\phi_n + \alpha_2(\phi_n - \delta_{n0}\mathfrak{F}[\phi_0]) = V_1[\mathcal{G}h_{1n}]. \tag{21}$$

The presence of the flux-surface-average is crucial for the proper $n = 0$ density response [31]. It is this reduced model that has received the most attention in numerical simulation for the study of ITG-ae modes. One minor point, peculiar to the $n = 0$ adiabatic case, is that the Poisson equation is not diagonal in θ. To obtain a numerical solution of the adiabatic model it is convenient to first solve the flux-surface-averaged equation,

$$\alpha_1(1 - \mathfrak{F}[\mathcal{R}])\mathfrak{F}[\phi_0] = \mathfrak{F}V_1[\mathcal{G}h_{1n}] \tag{22}$$

for $\mathfrak{F}[\phi_0]$. To a very good approximation, we have taken $\mathfrak{F}[\mathcal{R}\phi_0] \sim \mathfrak{F}[\mathcal{R}]\mathfrak{F}[\phi_0]$. No such approximation is required when the kinetic electron response is used. Knowing $\mathfrak{F}[\phi_0]$, we can then solve an equation for ϕ_0 which is diagonal in θ.

3.3. The Ampère equation

To describe transverse magnetic fluctuations we use the parallel component of Ampère's law ($\delta B_\parallel$ effects are generally negligible for the modes of interest and are ignored in this work). In terms of the distribution h we have

$$-\frac{2\rho_s^2}{\beta_e}\nabla_\perp^2 A_{\parallel n} = V_1[v_\parallel \mathcal{G}(h_{1n} - \alpha_1 v_{\parallel 1} A_{\parallel n})] - V_2[v_\parallel (h_{2n} + \alpha_2 v_{\parallel 2} A_{\parallel n})]. \tag{23}$$

Note that $V_1[v_{\parallel 1}^2] = T_1$ and $V_2[v_{\parallel 2}^2] = (m_1/m_2)T_2 \gg 1$. Since the notation is potentially confusing, we remind the reader that in a simulation where electron and ion temperatures are constant and equal, we have $T_1 = T_2 = 1$.

It has been known for many years that the Ampère equation, when written in the form of Eq. (23), is frustratingly difficult to solve numerically owing to a delicate cancellation in the electron current which occurs when $\beta_e > m_2/m_1$ – a condition that is well satisfied for experimentally relevant values of β_e. The nature of the cancellation is evident upon examination of the asymptotic balance of terms in Eq. (23) (take $k_r \to 0$ for simplicity)

$$\frac{2(k_\theta \rho_s)^2}{\beta_e} A_{\parallel n} \sim -V_2[v_{\parallel 2} h_{2n}] - V_2[v_{\parallel 2}^2 A_{\parallel n}]. \tag{24}$$

When $k_\theta \rho_s \sim 0.1$ and $\beta_e \sim 1\%$, the LHS of Eq. (24) is approximately $2A_{\parallel n}$, whereas the second velocity integral on the RHS is equal to $3600A_{\parallel n}$ for a deuterium plasma! The sobering implication is that that the two velocity integrals must cancel almost exactly, with the remainder determining the physics. This problem is made virtually intolerable in GK-PIC codes owing to the presence of a finite amount of discrete particle (statistical) noise. Various authors have reported that PIC solvers must resolve space scales on the order of the collisionless skin depth, $c/\omega_{pe} = \rho_s\sqrt{\beta(m_2/m_1)}$, to accurately describe finite-β_e dynamics. Methods to remedy this problem in PIC codes are under development [19–23]. In Eulerian codes, it has been recognized that the remedy is to ensure a term-by-term cancellation of the $O(m_1/m_2)$ terms in the electron current. This is normally accomplished by evaluating $V_2[v_\parallel^2 A_{\parallel n}]$ numerically using exactly the same discretization scheme as for $V_2[v_\parallel h_{2n}]$.

3.4. Model summary

In the interest of clarity, we summarize the different possible sets of model equations, in order of increasing sophistication.

3.4.1. Electrostatic with adiabatic electrons

Eq. (14) for h_1, plus Eq. (21) for ϕ.

3.4.2. Electrostatic with kinetic electrons

Eq. (14) for h_1 and h_2, plus Eq. (19) for ϕ.

3.4.3. Electromagnetic

Eq. (14) for h_1 and h_2, plus Eq. (19) for ϕ and Eq. (23) for $A_\parallel$.

4. Orbit-time grid for poloidal motion

Consider the motion due only to parallel advection (omitting the species index for brevity)

$$\frac{\partial h}{\partial t} + \frac{1}{R_0 q}\frac{v_\parallel(\theta)}{g_\theta(\theta)}\frac{\partial \bar{h}}{\partial \theta} = 0, \tag{25}$$

where $\bar{h} \doteq h + z\alpha u$. Eq. (25) is subject to short-wavelength numerical instability in regions where the variation of $v_\parallel(\theta)$ is sufficiently strong. This property is well known [32], and time-explicit schemes must normally include dissipative smoothing if a solution is sought on an equally spaced θ-grid. Moreover, at bounce points θ_b, where $v_\parallel(\theta_b) = 0$, the distribution function may develop cusps, bringing into question the accuracy of any finite-difference scheme on such a grid.

This leads us to the observation that the poloidal angle, θ, is a *poor* variable for numerical solution of the GK equation. The obvious solution is to remove these cusps analytically using the normalized *orbit time* for discretization in the poloidal direction. To this end, define

$$\tau_0(\lambda,\theta) \doteq \begin{cases} \displaystyle\int_{-\theta_b}^{\theta} \frac{g_\theta(\theta)\mathrm{d}\theta'}{\sqrt{1-\lambda\hat{B}(\theta')}} & \text{if } \lambda \leqslant \dfrac{1}{\hat{B}(\pi)} \text{(trapped)}, \\ \displaystyle\int_{-\pi}^{\theta} \frac{g_\theta(\theta)\mathrm{d}\theta'}{\sqrt{1-\lambda\hat{B}(\theta')}} & \text{if } \lambda > \dfrac{1}{\hat{B}(\pi)} \text{(passing)}, \end{cases} \tag{26}$$

where θ_b is the solution of $\hat{B}(\theta_b) = 1/\lambda$. $\tau_0(\lambda,\theta)$ must be computed numerically for general plasma equilibria – a tedious but straightforward exercise in numerical analysis. Note that in Eq. (26), and in the rest of this section, we suppress the radial dependence of $\tau_0(\lambda, r, \theta)$, $\hat{B}(r,\theta)$ and $g_\theta(r,\theta)$ for brevity.

Next, we introduce a normalized orbit time, τ, which runs from 0 to 2 for a given λ and describes *both signs of velocity*. In this way τ parameterizes the solution on both Riemann sheets by subsuming the two signs of velocity:

$$\tau(\lambda,\theta) \doteq \begin{cases} \tau_0(\lambda,\theta)/\bar{\tau}(\lambda) & \text{for } 0 \leqslant \tau \leqslant 1 \quad (\sigma = 1), \\ 2 - \tau_0(\lambda,\theta)/\bar{\tau}(\lambda) & \text{for } 1 < \tau \leqslant 2 \quad (\sigma = -1), \end{cases} \tag{27}$$

where $\bar{\tau}(\lambda) = \tau_0(\lambda,\theta_b)$ for trapped particles, and $\bar{\tau}(\lambda) = \tau_0(\lambda,\pi)$ for passing particles. The parallel advection operator is reduced to one with constant velocity

$$\frac{\partial h}{\partial t} + \Omega(\epsilon,\lambda)\frac{\partial \bar{h}}{\partial \tau} = 0, \quad \text{where } \Omega(\epsilon,\lambda) \doteq \sqrt{\frac{m_s}{m_1}}\frac{\sqrt{2\epsilon T_s}}{\bar{\tau}(\lambda)}. \tag{28}$$

High-accuracy numerical discretization schemes for this form of the equation are well documented. Boundary conditions on physical distributions can be stated very simply: trapped are periodic on the interval [0,2), co-passing are periodic on [0,1), and counter-passing are periodic on [1,2). However, the field-aligned coordinate system [see Eq. (11)] requires that the functions h describing the passing population are not periodic, but subject to phase conditions: $h(1) = \mathscr{P}h(0)$ for co-passing, and $h(2) = \mathscr{P}h(1)$ for counter-passing. The important result is that as a function of τ, the trapped distribution will be not only continuous, but also *smooth*, across bounce points no matter what order difference scheme is used. The obvious physical interpretation of the location of orbit-time gridpoints is that they are equally spaced in time, not space, along an orbit. In particular, because they are highly stagnant near $\theta = \pm\pi$, particles close to the trapped-passing boundary benefit from equal-time spacing.

For finite-n modes, it is possible to solve Eq. (28) with a centered 5-point, fourth-order difference discretization formula

$$\frac{\partial h_j}{\partial t} + \frac{\Omega}{12\Delta\tau}(-\bar{h}_{j+2} + 8\bar{h}_{j+1} - 8\bar{h}_{j-1} + \bar{h}_{j-2}) = 0, \tag{29}$$

such that $\Delta\tau \doteq 2/n_\tau$. Unfortunately, this form will give rise to numerical instability for sufficiently small values of n. A more robust form is obtained by adding a fourth-derivative smoother to Eq. (29).

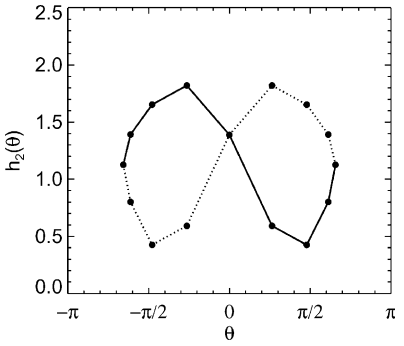

Fig. 1. Numerical calculation of the poloidal dependence of the electron distribution function, for fixed energy, pitch angle and radius. A third-order upwind scheme on an equally spaced τ-grid ($n_\tau = 16$) is used. Solid (dotted) line indicates $\sigma = 1$ ($\sigma = -1$). Note the divergence of $\partial h_2/\partial\theta$ at $\theta = \pm\theta_b$.

$$\frac{\partial h_j}{\partial t} + \frac{\Omega}{12\Delta\tau}(-\bar{h}_{j+2} + 8\bar{h}_{j+1} - 8\bar{h}_{j-1} + \bar{h}_{j-2}) = -\frac{|\Omega|}{12\Delta\tau}(h_{j+2} - 4h_{j+1} + 6h_j - 4h_{j-1} + h_{j-2}). \tag{30}$$

The scheme above is the well-known third-order upwind method. In addition to the elimination of low-n numerical instabilities, this upwind scheme will give proper Landau damping of $n = 0$ GAMs. Note that the dissipation, above, acts on h but not $\bar{h}$. In fact, attempting to add upwind diffusion to $\bar{h}$ (that is, also to fields) will generate a low-k_r numerical instability which worsens as the square of the *radial* box size. The difference scheme of Eq. (30) is exactly that used to discretize the parallel motion in Eq. (14). This is done at every radius, energy and pitch angle. A plot showing the θ-dependence of the electron distribution (obtained from a numerical solution of the full GKM equations) appears in Fig. 1. Although $\partial_\theta h$ is singular at bounce points, no grid instability is present.

5. Blending-function Maxwell solver

Since the distribution function h is computed at a different set of points $\{\theta_j\}$ for each discrete value of λ, there is no natural way to solve the Maxwell equations using finite-difference methods on a fixed poloidal grid. Instead, we adopt a *function-space* approach, and expand the fields $(\phi_n, A_{\|n})$ in series of *uniform polynomial blending functions*. We will show that basis functions which incorporate the complex phase conditions [see Eq. (12)] at $-\pi$ and π can be constructed from pairs of these blending functions. Equations for the expansion coefficients are then obtained using the well-known Galerkin method.

In computing the poloidal dependence of the fields, there are a number of separate discretization effects to consider. Since the fields are sums (integrals in the continuum limit) of distribution functions, low velocity-space resolution will lead to poor poloidal accuracy – even if the there are no other sources of discretization error. Conversely, even when a very large number of velocity-space grids are used, discretization error in the orbit-time integration of h_{sn} will lead to poor poloidal accuracy – even if the function-space method of the present section was exact. Thus, achieving an absolute level of accuracy in the θ-dependence of the fields requires sufficient convergence in both velocity-space and in orbit-time.

5.1. Examples of blending functions

A finite number of blending functions, $N_m(s)$, are used to provide a basis for the field expansion. An important feature of the N_m, however, is that they are all translates of a single function $N(s)$, such that $N(s - m) = N_m(s)$. In practise, we use one of the following three types of blending functions:

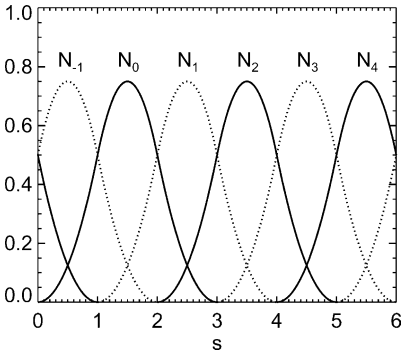

Fig. 2. Quadratic blending functions, $N_m^{(3)}(s)$, for $n_b = 6$.

Piecewise linear:

$$N^{(2)}(s) \doteq \begin{cases} s & \text{if } 0 \leqslant s \leqslant 1, \\ 2 - s & \text{if } 1 \leqslant s \leqslant 2. \end{cases} \tag{31}$$

Piecewise quadratic:

$$N^{(3)}(s) \doteq \begin{cases} s^2/2 & \text{if } 0 \leqslant s \leqslant 1, \\ -(3/2) + 3s - s^2 & \text{if } 1 \leqslant s \leqslant 2, \\ (3-s)^2/2 & \text{if } 2 \leqslant s \leqslant 3. \end{cases} \tag{32}$$

Piecewise cubic:

$$N^{(4)}(s) \doteq \begin{cases} (1/6)s^3 & \text{if } 0 \leqslant s \leqslant 1, \\ (2/3) - 2s + 2s^2 - (1/2)s^3 & \text{if } 1 \leqslant s \leqslant 2, \\ -(22/3) + 10s - 4s^2 + (1/2)s^3 & \text{if } 2 \leqslant s \leqslant 3, \\ (1/6)(4-s)^3 & \text{if } 3 \leqslant s \leqslant 4. \end{cases} \tag{33}$$

In Fig. 2 we give plots of $N_m^{(3)}$ for $m = -2, \ldots, 4$.

5.2. Representation of a quasi-periodic function

It remains to construct meaningful set of *basis* vectors from the prototype blending functions given above. Let us begin by considering a function $f(\theta)$ which is not periodic in θ, but satisfies a phase condition $f(\theta + 2\pi) = \mathscr{P} f(\theta)$. On the infinite domain $(-\infty, \infty)$ we can write

$$f(\theta) = \sum_{m=-\infty}^{\infty} c_m N_m(\theta/\Delta\theta), \tag{34}$$

$$= \sum_{m=1}^{n_b} [\cdots + c_{m-n_b} N_{m-n_b} + c_m N_m + c_{m+n_b} N_{m+n_b} + \cdots], \tag{35}$$

where $N_m(\theta/\Delta\theta) = N(\theta/\Delta\theta - m)$, $\Delta\theta \doteq 2\pi/n_b$, and n_b is the number of basis functions used to represent one 2π-segment of the function f. The phase condition in θ translates into an equivalent phase condition for the blending coefficients themselves; namely $c_{m+n_b} = \mathscr{P} c_m$. The function f is therefore completely described by the coefficients $\{c_1, \ldots, c_{n_b}\}$ and basis functions $\{F_1, \ldots, F_{n_b}\}$ according to

$$f(\theta) = \sum_{m=1}^{n_b} c_m F_m(\theta), \quad \text{where } F_m(\theta) = N(\theta/\Delta\theta - m) + \mathscr{P} N(\theta/\Delta\theta - m - n_b). \tag{36}$$

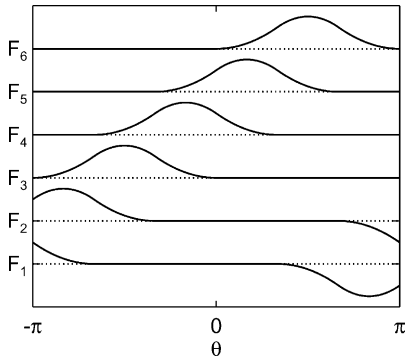

Fig. 3. Quadratic basis functions, $F_m(\theta)$, for $n_b = 6$ and phase $\mathscr{P} = -1$.

In choosing a value of the parameter n_b, one is constrained by the number of points used in the orbit time discretization, n_τ. Given that a passing particle is described by $n_\tau/2$ orbit points, choosing values of n_b larger than $n_\tau/2$ will lead to a breakdown of the method since there will be less than one orbit point per blending function segment. For the simulations presented in this paper, we have found that $n_b = 6$ and $n_\tau = 20$ are efficient choices. However, we expect that the simulation of plasmas with strong equilibrium shaping, will require a simultaneous increase of both n_b and n_τ.

Fig. 3 shows the $n_b = 6$ quadratic basis functions $\{F_1, \ldots, F_6\}$ for $\mathscr{P} = -1$. We remark that since $\mathscr{P}$ is generally a complex number, the basis functions are also complex. If the function $f(\theta)$ is known, then we can determine the c_m by demanding that the error is orthogonal to the space spanned by the $\{F_m\}$. That is, we multiply by F_m^* and integrate to obtain

$$c_m = (P^{-1})_{mm'} b_{m'} \quad \text{such that } b_m = \int_{-\pi}^{\pi} \mathrm{d}\theta F_m^*(\theta) f(\theta), \tag{37}$$

where P is the hermitian *projection matrix*.

$$P_{mm'} \doteq \int_{-\pi}^{\pi} \mathrm{d}\theta F_m^*(\theta) F_{m'}(\theta). \tag{38}$$

A few well known but important observations concerning the approximation properties of the linear, quadratic and cubic functions should be stated. In a region of extremely rapid field variation, the cubic approximation is the least robust – suffering from overshoot/undershoot oscillations. Conversely, as the fields become progressively smoother, the linear approximation will give the poorest interpolation accuracy. A further undesirable property of the linear approximation is its discontinuous first derivative. Although there is no general rule or obviously best interpolation order for all situations, we find that the piecewise quadratic functions are sufficiently accurate and robust for all cases studied to date.

5.3. Solution of the Maxwell equations

It will be convenient in what follows to abbreviate the radial operators which appear in the Maxwell equations as

$$\mathfrak{L}_P \doteq \alpha_1 (1 - \mathscr{R}), \tag{39}$$

$$\mathfrak{L}_A \doteq -\frac{2\rho_s^2}{\beta_e} \nabla_\perp^2. \tag{40}$$

In terms of these operators, the Maxwell equations become (omitting the toroidal mode index for brevity)

$$\mathfrak{L}_P\phi = V_1[\mathscr{G}h_1] - V_2[h_2], \tag{41}$$

$$\mathfrak{L}_A A_\parallel + \alpha_1 V_1[v_{\parallel 1}^2 A_\parallel] + \alpha_2 V_2[v_{\parallel 2}^2 A_\parallel] = V_1[v_{\parallel 1}\mathscr{G}h_1] - V_2[v_{\parallel 2}h_2]. \tag{42}$$

With the arguments of Section 3.3 in mind, it must be strongly emphasized that the third term on the LHS of Eq. (42) *must not be evaluated analytically*. That is, we must not set $V_2[v_\parallel^2 A_\parallel] = (m_1/m_2)T_2 A_\parallel$. Doing so will cause an imperfect cancellation with terms in $V_2[v_\parallel h_2]$, leading to an incorrect description of Alfvén waves. On the LHS of Eq. (42), we have also set $\mathscr{R} \to 1$. It is easy to show that this is roughly equivalent to a negligibly small shift in β_e. Begin by formally expanding both fields in blending series

$$\phi^i(\theta) = \sum_{m=1}^{n_b} \tilde{\phi}_m^i F_m^i(\theta), \tag{43}$$

$$A_\parallel^i(\theta) = \sum_{m=1}^{n_b} \tilde{A}_{\parallel m}^i F_m^i(\theta). \tag{44}$$

Substituting these into Eqs. (41) and (42), respectively, we find

$$\mathfrak{L}_P^{ii'}(\theta) \sum_m \tilde{\phi}_{m'}^{i'} F_{m'}^{i'}(\theta) = V_1[(\mathscr{G}h_1)^i] - V_2[h_2^i], \tag{45}$$

$$\begin{aligned}&\mathfrak{L}_A^{ii'}(\theta) \sum_m \tilde{A}_{\parallel m'}^{i'} F_{m'}^{i'}(\theta) + \alpha_1 V_1[(v_{\parallel 1}^i)^2 \sum_{m'} \tilde{A}_{\parallel m'}^i F_{m'}^i(\theta)] + \alpha_2 V_2[(v_{\parallel 2}^i)^2 \sum_{m'} \tilde{A}_{\parallel m'}^i F_{m'}^i(\theta)] \\ &\quad = V_1[v_{\parallel 1}^i (\mathscr{G}h_1)^i] - V_2[v_{\parallel 2}^i h_2^i].\end{aligned} \tag{46}$$

In order to obtain equations for the blending coefficients $\tilde{\phi}_m^i$ and $\tilde{A}_{\parallel m}^i$, we multiply Eqs. (45) and (46) by $F_m^i(\theta)^*$ and integrate over $[-\pi, \pi)$ to find

$$(M_P)_{mm'}^{ii'} \tilde{\phi}_{m'}^{i'} = (S_P)_m^i, \tag{47}$$

$$(M_A^1)_{mm'}^{ii'} \tilde{A}_{\parallel m'}^{i'} + (M_A^2)_{mm'}^i \tilde{A}_{\parallel m'}^i = (S_A)_m^i, \tag{48}$$

where

$$(M_P)_{mm'}^{ii'} = \int_{-\pi}^{\pi} \mathrm{d}\theta F_m^i(\theta)^* \mathfrak{L}_P^{ii'}(\theta) F_{m'}^{i'}(\theta), \tag{49}$$

$$(M_A^1)_{mm'}^{ii'} = \int_{-\pi}^{\pi} \mathrm{d}\theta F_m^i(\theta)^* \mathfrak{L}_A^{ii'}(\theta) F_{m'}^{i'}(\theta), \tag{50}$$

$$(M_A^2)_{mm'}^i = \alpha_1 \mathscr{J}_0 \mathfrak{F} V_1[(v_{\parallel 1}^i)^2 F_m^i(\theta)^* F_{m'}^i(\theta)/\mathscr{J}^i] - \alpha_2 \mathscr{J}_0 \mathfrak{F} V_2[(v_{\parallel 2}^i)^2 F_m^i(\theta)^* F_{m'}^i(\theta)/\mathscr{J}^i], \tag{51}$$

$$(S_P)_m^i = \mathscr{J}_0 \mathfrak{F} V_1[F_m^i(\theta)^* \mathscr{G}h_1^i/\mathscr{J}^i] - \mathscr{J}_0 \mathfrak{F} V_2[F_m^i(\theta)^* h_2^i/\mathscr{J}^i], \tag{52}$$

$$(S_A)_m^i = \mathscr{J}_0 \mathfrak{F} V_1\left[v_{\parallel 1}^i F_m^i(\theta)^* \mathscr{G}h_1^i/\mathscr{J}^i\right] - \mathscr{J}_0 \mathfrak{F} V_2\left[v_{\parallel 2}^i F_m^i(\theta)^* h_2^i/\mathscr{J}^i\right]. \tag{53}$$

The $\mathscr{J}_0$ factors in the moment formulae arise directly from the identity

$$\int_{-\pi}^{\pi} \mathrm{d}\theta f(\theta) = \mathscr{J}_0 \mathfrak{F}[f(\theta)/\mathscr{J}(\theta)] \tag{54}$$

with $\mathscr{J}$ and $\mathscr{J}_0$ defined in Eq. (3).

The matrices $(M_P)^{ii'}_{mm'}$ and $(M^1_A)^{ii'}_{mm'}$ which appear above are sparse in the radial index i. It is necessary to exploit this sparse structure to minimize computational time and storage. In `gyro` we solve the matrix problems for the desired blending coefficients $\tilde{\phi}$ and $\tilde{A}_\parallel$ using UMFPACK [33]. Discretization of the operators $\mathfrak{F}V_1$ and $\mathfrak{F}V_2$ is discussed in Section 6.

5.3.1. Alternative Poisson solver

In the solution of the Poisson equation, there is no analog of the delicate mass-ratio cancellation of Ampère's law. We may therefore use an alternative algorithm which retains the diagonal-in-θ nature of the continuous equation. An additional parameter, n_θ, is added to the overall scheme, which can be summarized thusly: (1) project velocity integrals (densities) onto the space of blending functions; (2) evaluate the blending representation of the densities at n_θ poloidal angles θ_j; (3) solve, at every θ_j, a radial matrix problem for the potential ϕ^i_j; (4) from the ϕ^i_j obtain a blending representation $\phi^i(\theta)$. The formulae to accomplish steps (1)–(3) are given by

$$\alpha_1\left(\delta^{ii'} - \mathscr{R}^{ii'}_j\right)\phi^{i'}_j = \delta n^i_j, \tag{55}$$

$$\delta n^i_j = \sum_{m=1}^{n_\mathrm{b}} \widetilde{\delta \boldsymbol{n}}^i_m F^i_m(\theta_j), \tag{56}$$

$$\widetilde{\delta \boldsymbol{n}}^i_m = (P^{-1})^i_{mm'}(S_P)^i_m, \tag{57}$$

where P is defined in Eq. (38), and S_P in Eq. (52). This is enough to compute ϕ^i_j at discrete angles θ_j. The final step proceeds by defining a continuous, piecewise-linear function $\hat{\boldsymbol{\phi}}^i(\theta)$ such that $\hat{\boldsymbol{\phi}}^i(\theta_j) = \phi^i_j$. Explicitly,

$$\hat{\boldsymbol{\phi}}^i(\theta) \doteq \left(\frac{\theta_{j+1} - \theta}{\Delta\theta}\right)\phi^i_j + \left(\frac{\theta - \theta_j}{\Delta\theta}\right)\phi^i_{j+1} \quad \text{for } \theta_j \leqslant \theta \leqslant \theta_{j+1}, \tag{58}$$

where $\Delta\theta \doteq 2\pi/n_\theta$. Then, the blending coefficients $\tilde{\boldsymbol{\phi}}^i_m$ are computed by inverting

$$\hat{\boldsymbol{\phi}}^i(\theta) = \sum_{m=1}^{n_\mathrm{b}} \tilde{\boldsymbol{\phi}}^i_m F_m(\theta). \tag{59}$$

The parameter n_θ is adjustable independently of all other grid dimensions. For simulations with adiabatic electrons and quadratic blending functions, it is possible although not advisable to do simulations with $n_\theta = n_\mathrm{b}$. An improvement in accuracy (important for electromagnetic simulations) is realized when doubling the resolution to $n_\theta = 2n_\mathrm{b}$. This is unsurprising, since there is some accuracy loss when using the linear interpolation defined by Eq. (58) with quadratic blending functions. An obvious generalization of this method (not implemented) is to use a quadratic interpolation with quadratic blending functions and a cubic interpolation with cubic blending functions, rather than Eq. (58) in all cases.

Finally, we remark that for realistic problem sizes, this alternative method is much faster than the full blending-space method of the previous section.

6. Numerical evaluation of FV

The Maxwell solvers of the previous section are written in terms of the operators $\mathfrak{F}V_1$ and $\mathfrak{F}V_2$. In the present section, we discuss quadrature methods for evaluation of these operators. Since the techniques which follow apply independently to both species, we omit species indices for brevity.

6.1. Decomposition of $\mathfrak{F}V$

Since $V[1] = 1$, it follows automatically that $\mathfrak{F}V[1] = 1$. An equivalent statement of this result is embodied in the identity

$$\frac{1}{2\sqrt{\pi}} \int_0^\infty \mathrm{d}\epsilon\, \mathrm{e}^{-\epsilon} \sqrt{\epsilon} \int_0^{\lambda^*} \mathrm{d}\lambda\, \bar{\tau}(\lambda) \oint \mathrm{d}\tau = \mathscr{J}_0 \tag{60}$$

with $\lambda^* = 1/\hat{B}(r,0)$ the maximum possible value of λ, and $\mathscr{J}_0$ defined in Eq. (2). Above, we have used the integral identity

$$\sum_\sigma \int_{-\pi}^{\pi} \mathrm{d}\theta\, g_\theta(r,\theta) \int_0^{1/\hat{B}(r,\theta)} \frac{\mathrm{d}\lambda}{\sqrt{1-\lambda\hat{B}(r,\theta)}} = \int_0^{\lambda^*} \mathrm{d}\lambda\, \bar{\tau}(\lambda) \oint \mathrm{d}\tau. \tag{61}$$

Since the numerical evaluation of integrals of this type will involve separate integration weights in each of the variables ϵ, λ and τ, it is useful to make the decomposition $\mathfrak{F}V = V_\epsilon \times V_\lambda \times V_\tau$, where

$$V_\epsilon[h] \doteq \frac{2}{\sqrt{\pi}} \int_0^\infty \mathrm{d}\epsilon\, \mathrm{e}^{-\epsilon} \sqrt{\epsilon} h, \tag{62}$$

$$V_\lambda[h] \doteq \frac{1}{2\mathscr{J}_0} \int_0^{\lambda^*} \mathrm{d}\lambda\, \bar{\tau}(\lambda) h, \tag{63}$$

$$V_\tau[h] \doteq \frac{1}{2} \oint \mathrm{d}\tau\, h. \tag{64}$$

These are normalized so that $V_\epsilon[1] = V_\lambda[1] = V_\tau[1] = 1$. The task at hand, now, is the construction of discrete forms of these operators, and therefore of $\mathfrak{F}V$.

6.2. Energy integration

To develop a quadrature method for the energy integral, we split the interval of integration in V_ϵ – defined in Eq. (62) – into two regions: $[0, \epsilon^*)$ and $[\epsilon^*, \infty)$, where ϵ^* is the maximum energy gridpoint (input). Integration over the first interval is done by changing variables according to

$$x(\epsilon) \doteq \frac{2}{\sqrt{\pi}} \int_0^\epsilon \mathrm{d}\epsilon\, \mathrm{e}^{-\epsilon} \sqrt{\epsilon}. \tag{65}$$

We let $x_0 \doteq x(\epsilon^*)$, and evaluate the integral using Gauss–Legendre integration [34] over $n_\epsilon - 1$ points

$$\int_0^{x_0} \mathrm{d}x\, h[\epsilon(x)] \simeq \sum_{i=1}^{n_\epsilon - 1} w_i h[\epsilon(x_i)]. \tag{66}$$

Table 2
Sample energy abscissae and weights

	$n_\epsilon = 4$, $\epsilon^* = 3.0$		$n_\epsilon = 6$, $\epsilon^* = 4.0$	
i	ϵ_i	w_i	ϵ_i	w_i
1	0.2924572707	0.2467749375	0.1625303849	0.1130127375
2	1.0404041729	0.3948399000	0.5442466206	0.2283030745
3	2.2531263847	0.2467749375	1.1228428641	0.2713566704
4	3.0000000000	0.1116102251	1.9784353093	0.2283030745
5			3.2361246631	0.1130127375
6			4.0000000000	0.0460117057

The abscissae and weights (x_i, w_i) are the usual Gauss–Legendre ones. Note that we must solve the nonlinear equations $x_i = x(\epsilon_i)$ for ϵ_i to obtain the energy gridpoints. With the dominant part of the energy integration done, we evaluate the remaining, infinite integral according to

$$\frac{2}{\sqrt{\pi}} \int_{\epsilon^*}^{\infty} \mathrm{d}\epsilon\, \mathrm{e}^{-\epsilon} \sqrt{\epsilon} h(\epsilon) \simeq h(\epsilon^*) \frac{2}{\sqrt{\pi}} \int_{\epsilon^*}^{\infty} \mathrm{d}\epsilon\, \mathrm{e}^{-\epsilon} \sqrt{\epsilon} = (1 - x_0) h(\epsilon^*). \tag{67}$$

This gives the final weight $1 - x_0$ at the energy gridpoint ϵ^*, for a total of n_ϵ gridpoints. We remark that this method has the desirable property

$$\sum_{i=1}^{n_\epsilon} w_i = 1 \quad \text{such that } \forall i, w_i > 0. \tag{68}$$

Some sample abscissae and weights are given in Table 2 to limited precision (10 significant digits). Note that it is straightforward to generate these, and thus to enforce the sum in Eq. (68), to machine precision. The abcissae and weights are unique for a given n_ϵ and ϵ^*. Outside of this section, to avoid ambiguity, we will use index i_ϵ and weight $w_{i_\epsilon}^{(\epsilon)}$ to refer to energy integration.

6.3. λ integration

The λ integration follows essentially the same strategy as the energy integration, with only minor differences. First, introduce the integration variable

$$x(\lambda) \doteq \frac{1}{\mathscr{J}_0} \int_0^{\lambda} \mathrm{d}\lambda' \, \overline{\tau}(\lambda'). \tag{69}$$

Then, then V_λ can be expressed as

$$V_\lambda[h] = \int_0^1 \mathrm{d}x\, h[x(\lambda)]. \tag{70}$$

Because h is rapidly varying across the trapped-passing boundary at $x_\mathrm{t} = x(\lambda_\mathrm{t})$, where $\lambda_\mathrm{t} = 1/B(\pi)$, it is wise to split the previous integral into two regions

$$\int_0^1 \mathrm{d}x\, h[x(\lambda)] = \int_0^{x_\mathrm{t}} \mathrm{d}x\, h[x(\lambda)] + \int_{x_\mathrm{t}}^1 \mathrm{d}x\, h[x(\lambda)]. \tag{71}$$

Gauss–Legendre rules are then applied to each integral separately to determine abscissae and weights (x_i, w_i). Then, as before, the equations $x_i = x(\lambda_i)$ must be inverted numerically to obtain the gridpoints λ_i.

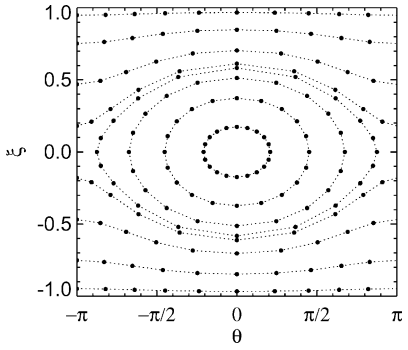

Fig. 4. Gridpoint distribution in the (θ, ξ)-plane, where $\xi \doteq v_\parallel / v$. Grid dimensions are $n_{\text{pass}} = n_{\text{trap}} = 4$ and $n_\tau = 20$.

Table 3
Sample λ weights for $n_{\text{pass}} = n_{\text{trap}} = 3$

i	x_i	λ_i	w_i
1	0.0701916516	0.1353809983	0.1730025988
2	0.3114046777	0.5237287429	0.2768041580
3	0.5526177038	0.7871934230	0.1730025988
4	0.6653193692	0.8581589333	0.1047751790
5	0.8114046777	0.9778736670	0.1676402866
6	0.9574899862	1.1217887702	0.1047751790

We emphasize that there is no assumption of continuity across the trapped passing boundary. In fact, in the collisionless limit, we do not expect the distribution to be continuous there. With weak collisions, we expect the formation of of a boundary layer around $x = x_{\text{t}}$. In the latter case, we expect good layer resolution because the Gauss–Legendre scheme puts integration abcissae very close to (but not on) x_{t}. When combined with the orbit-time grid, the λ integration abcissae provide the $(\lambda, v_\parallel / v)$ gridpoint distribution shown in Fig. 4.

Sample values of abscissae and weights are given in Table 3 for a circular equilibrium with $r/R_0 = 1/6$. Outside of this section, to avoid ambiguity, we will use index i_λ and weight $w_{i_\lambda}^{(\lambda)}$ to refer to pitch-angle integration.

6.4. Discretization summary

Our methods for solution of the Maxwell equations have the implication that it is not V but $\mathfrak{F}V$ for which a discrete form is required. But we have already done enough to show that the discretization takes the form

$$\mathfrak{F}V[h] \to \sum_{i_\epsilon=1}^{n_\epsilon} w_{i_\epsilon}^{(\epsilon)} \sum_{i_\lambda=1}^{n_\lambda} w_{i_\lambda}^{(\lambda)} \sum_{i_\tau=1}^{n_\tau} w_{i_\tau}^{(\tau)} h_{i_\epsilon i_\lambda i_\tau}, \tag{72}$$

where, so far, no radial discretization has been employed. The τ-weights are simply $w_{i_\tau}^{(\tau)} = (1/2)\Delta\tau = 1/n_\tau$. The numerical representation of the weights is such that when $h = 1$, the sum in Eq. (72) is unity to machine precision.

7. Radial discretization

7.1. Choice of radial box

For nonlinear simulations, the most general criterion for radial box selection is convergence of turbulent diffusivity with increasing box length. For linear and nonlinear flux-tube simulations, however, we can employ a more systematic method for choosing the radial box size. In a linear flux-tube simulation with $q_0 = q(r_0)$, $k_\theta = nq_0/r_0$, and nonzero magnetic shear, the most unstable ballooning mode has potential functions ϕ_n and $A_{\|n}$ which are radially periodic with wavelength $\ell_0 = 1/(|s|k_\theta)$. We can illustrate the origin of the length ℓ_0 by a brief consideration of the ballooning transform [35]. Begin by writing the potential for a single toroidal harmonic, and expand $q(r)$ about $r = r_0$

$$\phi(\varphi, r, \theta) = \mathrm{e}^{-\mathrm{i}n(\varphi - q\theta)}\phi_n(r,\theta) \sim \mathrm{e}^{-\mathrm{i}n(\varphi - q_0\theta) + \mathrm{i}\theta(r-r_0)/\ell_0}\phi_n(r,\theta). \tag{73}$$

Next, write ϕ_n as a Fourier series

$$\phi_n(r,\theta) = \sum_p \phi_p(\theta)\,\mathrm{e}^{2\pi\mathrm{i}p(r-r_0)/\ell_0}\mathrm{e}^{\mathrm{i}\theta_0(r-r_0)/\ell_0}, \tag{74}$$

where θ_0 is the so-called *ballooning angle*. Note that when $\theta_0 = 0$, the function ϕ_n is periodic on $r - r_0 \in [0, \ell_0]$. When $\theta_0 = \pi$, ϕ_n is periodic on $r - r_0 \in [0, 2\ell_0]$, and so on. For our present purposes, it is enough to consider the most unstable mode for which $\theta_0 = 0$. Generalization to arbitrary θ_0 is trivial. Upon introducing the ballooning potential

$$\phi_B(\theta + 2\pi p) \doteq \phi_p(\theta)\mathrm{e}^{-\mathrm{i}nq_0 2\pi p} \tag{75}$$

it follows that the physical potential has the form

$$\phi(\varphi, r, \theta) = \sum_p \mathrm{e}^{-\mathrm{i}n(\varphi - q_0\theta_p)}\mathrm{e}^{\mathrm{i}\theta_p(r-r_0)/\ell_0}\phi_B(\theta_p). \tag{76}$$

Above, $\theta_p \doteq \theta + 2\pi p \in [-\infty, \infty]$. This validates our assertion that for the most unstable linear mode, it is natural to employ a radial box of length ℓ_0. Nonlinear simulations, of course, cannot be restricted to $\theta_0 = 0$ and so much larger boxes are generally required. For the nonlinear simulations presented herein, we have used $\ell = 24\ell_0$, where ℓ_0 is set by the reference mode $k_\theta\rho_\mathrm{s} = 0.3$. We will discuss the consequences of these choices in more detail later. Note that this selection method arose primarily for historical reasons, and we reiterate the point that for nonlinear simulations, one must inevitably increase the box size until the diffusion in the radial region of interest becomes independent of size.

In the sections that follow, we define and discuss the discretization of all radial operators used in `gyro`.

7.2. Derivative operators

The *differential band width* in the radial direction is denoted by the parameter i_d. First and second derivatives can be discretized using n_d-point centered differences, where $n_d \doteq 2i_d + 1$. These are

$$\mathscr{D}_1^{ii'} f^{i'} = \frac{1}{\Delta r}\sum_{v=-i_d}^{i_d} c_{1v} f^{i+v}, \tag{77}$$

$$\mathscr{D}_2^{ii'} f^{i'} = \frac{1}{(\Delta r)^2}\sum_{v=-i_d}^{i_d} c_{2v} f^{i+v}, \tag{78}$$

where

$$c_1 v = \sum_{p\neq v} \frac{1}{v-p} \prod_{j\neq v,p} \frac{(-j)}{v-j}, \tag{79}$$

$$c_2 v = \sum_{p\neq v} \frac{1}{v-p} \sum_{q\neq v,p} \frac{1}{v-q} \prod_{j\neq v,q,p} \frac{(-j)}{v-j}. \tag{80}$$

The parameter n_d controls the formal truncation error of the difference approximation. This is $\mathrm{O}[(\Delta r)^{n_d-1}]$ for both the $\mathscr{D}_1$ and $\mathscr{D}_2$. For the first derivative appearing in the nonlinear terms, and in the Laplace operator in the Ampère equation, we set $\partial_r \to \mathscr{D}_1^{ii'}$. The second derivative appears only in the Ampère equation, and for that we set $\partial_{rr} \to \mathscr{D}_2^{ii'}$. It is well known, however, that ensuring the quality of a difference scheme requires more than a simple-minded consideration of truncation error. This is especially true for discretization of advection equations, where the addition of dissipation adds greatly to the numerical fidelity of the scheme (see, for example, Section 10 in connection with axisymmetric modes). Indeed, we have found that adding upwind dissipation to radial advection terms is required to smooth over sub-grid-scale numerical disturbances associated with electron Landau layer physics. Experience with implicit linear codes like `gks` have shown that accurate calculation of eigenvalues for low-frequency modes often does not require resolution of this layer. Analogously, `gks` solves the layer resolution problem by truncating allowed radial wavenumbers via zero boundary conditions in ballooning-angle. In both codes, it is found that as resolution is increased (as the radial grid is refined in `gyro`, or as the `gks` boundary conditions are moved outward in ballooning angle) the eigenvalue is invariant. That being said, there are case (for high β or close to marginal stability) where a very fine radial grid must be used.

To construct an arbitrary-order upwind scheme, we begin by writing the centered (n_d-1)th derivative as

$$\mathscr{D}_*^{ii'} f^{i'} = -\frac{1}{(\Delta r)^{n_d-1}} \sum_{v=-i_d}^{i_d} (-1)^v \binom{n_d-1}{v+i_d} f^{i+v}. \tag{81}$$

Discretization of the advective radial derivative in Eq. (14) then proceeds according to

$$v\partial_r \to v\mathscr{D}_1^{ii'} - \gamma|v|\mathscr{D}_*^{ii'}, \quad \text{where } \gamma \doteq |c_{1i_d}|(\Delta r)^{n_d-2}. \tag{82}$$

The overall normalization for the dissipation, γ, is chosen so as to recover the usual first and third-order upwind schemes. Setting $v=1$, we consider the action of this discretization on a pure wave,

$$(D_1 - \gamma D_*)\,\mathrm{e}^{\imath kr} = \imath K(k)\,\mathrm{e}^{\imath kr}. \tag{83}$$

While the exact result is evidently $K(k)=k$, the discretization yields a complex K which satisfies $\lim_{k\to 0} K/k = 1$. Curves of $\mathrm{Re}K(k)$ and $\mathrm{Im}K(k)$ are shown in Figs. 5 and 6, respectively for $\Delta r = 1$ and $n_d = 3,5,7,9$. Some comments regarding interpretation of these results is in order. Consider 100 gridpoints in a $100\rho_s$ box (i.e., $\Delta r = \rho_s$). A spectral approximation will interpret any grid-to-grid oscillation as a wave with $k_r\rho_s = \pi$. Fig. 5 shows that one can achieve essentially the same accuracy with an $n_d = 9$ finite-difference approximation using 128 gridpoints. The $n_d = 9$ derivative maintains good accuracy up to about $k_r\rho_s = 0.75\pi$, and by increasing the density of gridpoints by a factor of 128/100, we can describe waves up to $k_r\rho_s \sim \pi$. Moreover, very large boxes will benefit greatly from the locality of finite-difference operators.

Note that the $n_d = 5$ result corresponds to the upwind scheme of Section 4. In general, we never use $n_d = 3$ because of the very strong artificial damping of long waves ($k < \pi/2$) as shown by the dotted curve in Fig. 6.

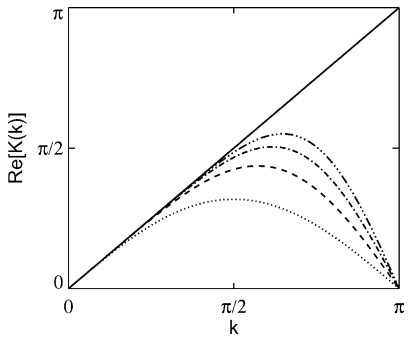

Fig. 5. Wavenumber dependence of finite-difference derivatives, $\mathscr{D}_1$, for $n_d = 3, 5, 7, 9$. The thick line shows the exact result. Larger values of n_d have higher maxima.

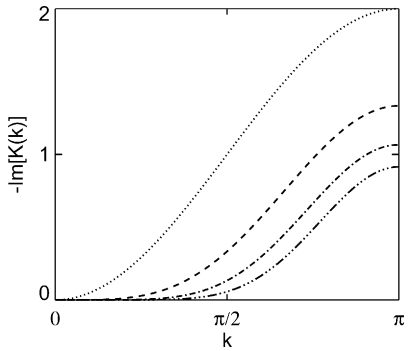

Fig. 6. Wavenumber dependence of the dissipation operator, $\gamma\mathscr{D}_*$, for $n_d = 3, 5, 7, 9$. Larger values of n_d have smaller maximum dissipation.

7.3. The gyro-operators

We have had very good results using truncated pseudospectral representations for the operators $\mathscr{G}$ and $\mathscr{R}$, even when the radial domain is nonperiodic. The validity of this method relies on the observation that the numerical contribution to the gyroaverage decays rapidly at distances beyond a few gyroradii from the gyrocenter. For linear benchmarks, when the radial domain is only one period of the ballooning mode, we generally use the fully pseudospectral representation with $n_g = n_r$ for $\mathscr{G}$ and $\mathscr{R}$. Here, $n_g \leqslant n_r$ is the number points in the gyro-operator stencil.

Analytically, the gyroaverage is an integral operator which acts on a field, $f(r, \theta, \varphi)$ as

$$\mathscr{G}f = \frac{1}{2\pi} \oint \mathrm{d}\vartheta \sum_n f_n(r'(\vartheta), \theta'(\vartheta))\, \mathrm{e}^{-\imath n\zeta'(\vartheta)}, \tag{84}$$

where the primed coordinates are evaluated along a gyro-orbit. The integration variable ϑ is the gyro-angle. The ϑ-variation of θ' in the integrand is dominated by the rapidly varying exponential, and in the gyrokinetic ordering it is consistent to set $\theta'(\vartheta) = \theta$ in f_n. If we further linearize the arguments in $\rho_\perp$, then the desired integral is

$$(\mathscr{G}f)_n = \frac{1}{2\pi} \oint \mathrm{d}\vartheta f_n(r + \rho_\perp |\nabla r| \cos\vartheta, \theta)\, \mathrm{e}^{-\imath n\rho_\perp(\zeta_x \cos\vartheta + \zeta_y \sin\vartheta)}, \tag{85}$$

where $\zeta_y \doteq k_\theta g_q$, $\zeta_x = [[k_x/k_y]]\zeta_y$ and $\rho_\perp = \rho_s\sqrt{2\epsilon\lambda\hat{B}T}/(g_r\hat{B})$ (see Section 2). If f_n is Fourier decomposed radially (assume for the moment that f_n is L-periodic in r) according to

$$(f_n)^i = \sum_{p=-J}^{J-1} (\widetilde{f}_n)^p \, \mathrm{e}^{2\pi\imath p r_i/L} = \sum_{p=-J}^{J-1} \mathscr{K}_{ip} (\widetilde{f}_n)^p, \quad \text{where } (\mathscr{K}^{-1})_{ip} = \frac{1}{2J}\mathscr{K}^\dagger_{ip} \tag{86}$$

with $J \doteq n_r/2$, then the gyroaveraging can be computed in a straightforward way. Evidently,

$$(\mathscr{G}f)^i_n = \sum_{p=-J}^{J-1} \mathrm{e}^{2\pi\imath p r_i/L} J_0\left(k^i_p \rho_\perp\right)(\widetilde{f}_n)^p, \tag{87}$$

where

$$k^i_p = \sqrt{(2\pi p|\nabla r|^i/L - \zeta^i_x)^2 + (\zeta^i_y)^2}. \tag{88}$$

When $n_\mathrm{g} < n_r$, it is convenient to define the truncation in terms of the *gyroaverage band width*, i_g. This number is increased until results converge to desired accuracy. For a typical $100\rho_\mathrm{s}$ box and instabilities with $k_\parallel \rho_s < 0.7$, converged results are obtained with the choices $n_r \sim 128$ and $i_\mathrm{g} \sim 6$.

$$\mathscr{G}^{ii'}_n = \begin{cases} \frac{1}{2J}\sum_{p=-J}^{J-1} z_p^{i-i'} J_0(k^i_p\rho_\perp) & \text{if } |i-i'| \leqslant i_\mathrm{g}, \\ 0 & \text{if } |i-i'| > i_\mathrm{g}, \end{cases} \tag{89}$$

$$\mathscr{R}^{ii'}_n = \begin{cases} \frac{1}{2J}\sum_{p=-J}^{J-1} z_p^{i-i'} \mathrm{e}^{-b^i_p} I_0(b^i_p) & \text{if } |i-i'| \leqslant i_\mathrm{g}, \\ 0 & \text{if } |i-i'| > i_\mathrm{g} \end{cases} \tag{90}$$

with $z_p = \exp(\imath\pi p/J)$, $(\mathscr{G}f)^i_n \doteq \mathscr{G}^{ii'}_n f^{i'}_n$, and $b_p = (\rho_s k_p\sqrt{T}/g_r\hat{B})^2$. J_0 is a Bessel function of the first kind, and I_0 is a modified Bessel function of the first kind.

7.4. Nonperiodic boundary conditions

Flux-tube boundary conditions effectively eliminate the inner and outer radial boundaries by making the quantities $(\phi_n, A_{\parallel n}, h_{sn})$ periodic in r. For example,

$$\phi_n(r_1,\theta) = \phi_n(r_2,\theta). \tag{91}$$

Use of this boundary condition is very useful for local linear analyses (all the linear results presented in this report use flux-tubes) and computationally efficient for restricted nonlinear studies. However, the flux-tube mode of operation is incompatible with variation of the equilibrium profiles. In order to study physical effects associated with profile variation, it is necessary to abandon flux-tubes and use some type of nonperiodic radial boundary condition. In the design of nonperiodic end conditions, we have attempted to minimize as much as possible the effect of the boundaries on the interior dynamics. To this extent, our goal was to construct 'benign'' rather than physical end conditions. The latter is a challenging problem for future work.

In Section 10 we discuss the performance of these boundary conditions, and show that they yield the same interior levels of diffusivity as flux-tubes when profiles are held constant.

To solve the equations in a radially nonperiodic annulus, we divide the full domain into various subdomains.

- Evanescent Region ($r < r_{\mathrm{Le}}, r > r_{\mathrm{Re}}$)
  h and $(\phi, A_\parallel)$ are taken to be evanescent. For example, h is given by

$$h(r) = \begin{cases} h(r_{\mathrm{Le}})e^{-c_1(r_{\mathrm{Le}}-r)} & \text{if } r < r_{\mathrm{Le}} \\ h(r_{\mathrm{Re}})e^{-c_1(r-r_{\mathrm{Re}})} & \text{if } r > r_{\mathrm{Re}} \end{cases} \tag{92}$$

  with completely analagous formulae for $(\phi, A_\parallel)$. We have had good results with $c_1 \sim 1/\Delta r$.
- Buffer Region ($r < r_{\mathrm{Lb}}, r > r_{\mathrm{Rb}}$)
  h is again taken to be evanescent,

$$h(r) = \begin{cases} h(r_{\mathrm{Lb}})e^{-c_1(r_{\mathrm{Lb}}-r)} & \text{if } r < r_{\mathrm{Lb}} \\ h(r_{\mathrm{Rb}})e^{-c_1(r-r_{\mathrm{Rb}})} & \text{if } r > r_{\mathrm{Rb}} \end{cases} \tag{93}$$

  but $(\phi, A_\parallel)$ are obtained from the Maxwell equations.
- Damping Region ($r < r_{\mathrm{Ld}}, r > r_{\mathrm{Rd}}$)
  In this region, a Krook-type artificial damping term, $-\nu_{\mathrm{d}} h$, is added to the RHS of the GK equations. This is only necessary for axisymmetric modes to inhibit the development of shear layers. $(\phi, A_\parallel)$ are obtained, without any added dissipation, from the Maxwell equations.
- Interior region ($r_{\mathrm{Ld}} < r < r_{\mathrm{Rd}}$)
  Inside the "clean" computational region, h is calculated from the gyrokinetic equations, and $(\phi, A_\parallel)$ from the Maxwell equations. No artificial effects are added.

Geometrically, these regions are embedded such that $r_{\mathrm{Rd}} < r_{\mathrm{Rb}} < r_{\mathrm{Re}}$ and $r_{\mathrm{Le}} < r_{\mathrm{Lb}} < r_{\mathrm{Ld}}$. See Section 10 for further discussion.

8. Nonlinear dynamics

8.1. Discretization scheme

Our experience has shown that numerical stability and robustness for the nonlinear problem can be enhanced by treating the discrete form of the nonlinear terms in a "conservative" manner. First, let us begin by writing the continuous form of the bracket appearing in Eq. (14)

$$\{F, G\} = \frac{\partial F}{\partial \alpha}\frac{\partial G}{\partial r} - \frac{\partial G}{\partial \alpha}\frac{\partial F}{\partial r}, \tag{94}$$

where F and G are arbitrary phase-space functions. To make contact with Eq. (14), we set $F \to \mathcal{G}u$ and $G \to h$. When the angle α is represented by a finite Fourier series, the bracket becomes

$$\{F, G\}_n = \sum_{n'} \left(n' F_{n'} \frac{\partial G_{n-n'}}{\partial r} - n' G_{n'} \frac{\partial F_{n-n'}}{\partial r} \right). \tag{95}$$

However, as an alternative to Eq. (94), we can write the bracket in conservative form

$$\{F, G\} = \frac{\partial}{\partial \alpha}\left(F \frac{\partial G}{\partial r} \right) - \frac{\partial}{\partial r}\left(F \frac{\partial G}{\partial \alpha} \right). \tag{96}$$

This has Fourier components

$$\{F, G\}_n = \sum_{n'} \left[n F_{n'} \frac{\partial G_{n-n'}}{\partial r} - n' \frac{\partial}{\partial r}(F_{n-n'} G_{n'}) \right]. \tag{97}$$

It is desirable to start with this form prior to performing the radial discretization. In terms of the discrete form of the derivative operator, $\mathscr{D}_1$, the discrete form of the nonlinear operator is

$$\{F,G\}_n^i = \sum_{n'}\left[nF_{n'}^i\mathscr{D}_1^{ii'}G_{n-n'}^{i'} - n'\mathscr{D}_1^{ii'}\left(F_{n-n'}^{i'}G_{n'}^{i'}\right)\right]. \tag{98}$$

This is the expression used in `gyro`. Now, let us assume, in what follows, that the radial domain is periodic. Deviations from the results below will as a consequence be solely limited to boundary effects. The lowest integral invariant, which measures the rate of change of density along the nonlinear flow, is

$$\int \mathrm{d}\alpha \int \mathrm{d}r\{F,G\} \to \sum_i \{F,G\}_0^i. \tag{99}$$

Using Eq. (98), the sum above vanishes for all $\mathscr{D}_1$ which satisfy $\sum_i \mathscr{D}_1^{ii'}a^{i'} = 0$ for all vectors a. Centered-difference formulae of all orders for $\mathscr{D}_1$, as summarized in Section 7, will satisfy this condition. The next invariant, connected with the rate of change of entropy, is

$$\int \mathrm{d}\alpha \int \mathrm{d}rG\{F,G\} \to \sum_n \sum_i G_{-n}^i\{F,G\}_n^i. \tag{100}$$

Some algebra gives (without assumption of a product rule for $\mathscr{D}_1$),

$$\sum_n \sum_i G_{-n}^i\{F,G\}_n^i = -\sum_{n,n'} n'\left[G_{-n}^i\mathscr{D}_1^{ii'}\left(F_{n-n'}^{i'}G_{n'}^{i'}\right) + F_{n-n'}^i G_{n'}^i\mathscr{D}_1^{ii'}G_{-n}^{i'}\right]. \tag{101}$$

This sum vanishes for all $\mathscr{D}_1$ which satisfy

$$\sum_i a^i\mathscr{D}_1^{ii'}b^i + b^i\mathscr{D}_1^{ii'}a^{i'} = 0 \quad \forall a,b. \tag{102}$$

Once again, centered difference operators of all orders will satisfy this constraint. Although the order of $\mathscr{D}_1$ is chosen at run-time, we typically use a 7-point (sixth order) rule. We have found that discretization schemes which leave residuals in Eqs. (99) and (100) were generally much more susceptible to numerical instability than the conservative methods.

8.2. Definitions of fluxes and diffusivities

One of the primary goals of `gyro` is to compute nonlinear, self-consistent fluxes and diffusivities for given parameters and toroidal equilibria. For each species separately, we define the $\mathbf{E}\times\mathbf{B}$ flux (superscript "es") as

$$\begin{pmatrix}\Gamma_n^{\mathrm{es}}(r,\theta)\\ \Gamma_{\mathrm{T}}^{(\mathrm{es})}(r,\theta)\end{pmatrix} = \imath\sum_n \frac{k_\theta\rho_{\mathrm{s}}}{g_r}\phi_n^*(r,\theta)V\left[\begin{pmatrix}1\\ \epsilon T\end{pmatrix}(\mathscr{G}h)_n\right] \tag{103}$$

and magnetic flutter (superscript "em") flux as

$$\begin{pmatrix}\Gamma_n^{\mathrm{em}}(r,\theta)\\ \Gamma_{\mathrm{T}}^{(\mathrm{em})}(r,\theta)\end{pmatrix} = -\imath\sum_n \frac{k_\theta\rho_{\mathrm{s}}}{g_r}A_{\parallel n}^*(r,\theta)V\left[\begin{pmatrix}1\\ \epsilon T\end{pmatrix}v_\parallel(\mathscr{G}h)_n\right]. \tag{104}$$

The subscripts n and T indicate particle and thermal fluxes, respectively. For each species separately, and for electrostatic and electromagnetic components separately, we write the gyroBohm-scaled particle and thermal diffusivities as

$$D(r) \doteq \frac{D^{\mathrm{p}}}{(c_{\mathrm{s}}/a)\rho_{\mathrm{s}}^2} = \frac{\mathfrak{F}[\Gamma_n]/(n/L_n)}{(c_{\mathrm{s}}/a)\rho_{\mathrm{s}}^2}, \tag{105}$$

$$\chi(r) \doteq \frac{\chi^{\mathrm{p}}}{(c_{\mathrm{s}}/a)\rho_{\mathrm{s}}^2} = \frac{\mathfrak{F}[\Gamma_{\mathrm{T}}]/(nT/L_T)}{(c_{\mathrm{s}}/a)\rho_{\mathrm{s}}^2}. \tag{106}$$

Above, D^{p} and χ^{p} are the physical diffusivities. In this report, we normally quote radial averages of the diffusivity, $\bar{D}^{\mathrm{p}}$ and $\bar{\chi}^{\mathrm{p}}$.

9. Time advance method

With all spatial operators discretized, and the fields $(\phi, A_{\parallel})$ considered as functionals of h_1 and h_2, we are left with a very large system of coupled ordinary differential equations (ODEs) for the totality of all distribution functions at all gridpoints. This is solved as an initial value problem

$$\frac{\mathrm{d}\vec{h}}{\mathrm{d}t} = \vec{\mathrm{U}}(\vec{h}), \quad \vec{h}(t_0) = \vec{h}_0 \quad \text{with } t \in [t_0, t_1]. \tag{107}$$

Here, $\vec{h} \doteq h_{\mathrm{s},n,i,i_\epsilon,i_\lambda,i_\tau}$ and $\vec{\mathrm{U}} \doteq \mathrm{RHS}_{\mathrm{s},n,i,i_\epsilon,i_\lambda,i_\tau}$. The MOL approach is particularly attractive since we can choose from a large number of very powerful, well studied, high-order ODE integrators to march Eq. (107) forward in time. For the results presented in this paper, we use the explicit Runge–Kutta (ERK) method RK4(3)5[2R+]C (with fixed timestep) as described in [36]. This is a five-stage, fourth-order accurate scheme with good linear stability properties (high advective and viscous Courant limits), good nonlinear stability (contractivity) properties, and an embedded third-order method to monitor the time-integration error. We find that the benefits of error-estimation more than justify the added cost associated with computing an extra stage. In general, ERK methods are suitable only for the collisionless part of the problem. Collisions are treated using operator splitting, as described in the next section.

The benefits of ERK methods become especially apparent when considering nonlinear problems. Both the $\mathbf{E} \times \mathbf{B}$ and magnetic flutter nonlinearities are computed with full fourth-order accuracy in time.

10. Adiabatic electron benchmarks

10.1. Definition of parameter sets

For benchmarking and testing we nominally use either the *Cyclone DIII-D base case* [34] or the *Waltz standard case* [7] parameter sets. There are summarized in Tables 4 and 5 respectively. All calculations in this report were performed using the $s - \alpha$ model equilibrium with $\alpha_{\mathrm{MHD}} = 0.0$ and $1/\hat{B} \to 1$ in $\omega_{\mathrm{ds}}^{(1)}$. Also, for simplicity we have set $T_1 = T_2$ throughout.

Table 4
Cyclone DIII-D base case parameter set

r/a	R_0/a	R_0/L_n	R_0/L_T	q	s
0.5	2.78	2.2	6.9	1.4	0.8

Table 5
Waltz standard case parameter set

r/a	R_0/a	R_0/L_n	R_0/L_T	q	s
0.5	3.0	3.0	9.0	2.0	1.0

10.2. Linear ITG modes

For the adiabatic electron model, we show complete agreement with the `gs2` code [17] for the calculation of Cyclone DIII-D base case ITG modes. This comparison is given in Figs. 7 and 8.

10.3. Rosenbluth–Hinton residual flows

We compare a numerical calculation of the time evolution of the axisymmetric potential with the results of Hinton and Rosenbluth [38,39]. They have shown that a rigorous initial value calculation leads to decaying oscillations of geodesic acoustic modes (GAMs) with finite residual potential. The GAM frequency and damping rate are given by

$$\omega_G = \left(\frac{7}{4}+\frac{T_2}{T_1}\right)^{1/2}\frac{v_1}{R} \quad \text{and} \quad v_G = -\omega_G e^{-q^2}, \tag{108}$$

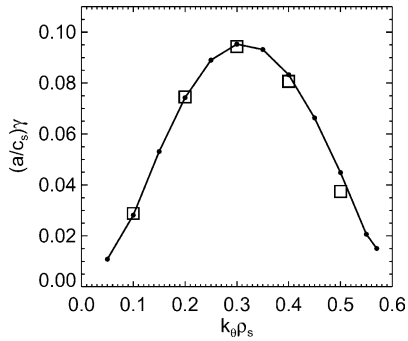

Fig. 7. Linear mode growth rates versus $k_\theta\rho_s$ for the Cyclone DIII-D base case. Curves are `gyro` results, squares are results from Dorland's `gs2` code.

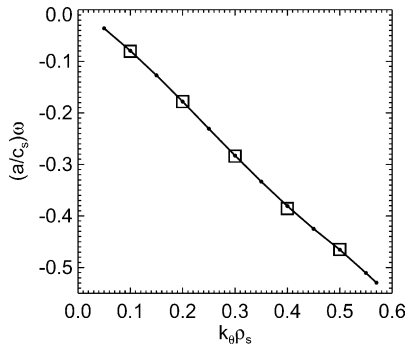

Fig. 8. Same as previous figure, but showing frequency comparison.

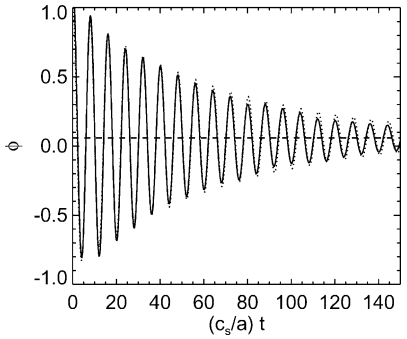

Fig. 9. Numerical calculation of axisymmetric poloidal flow (solid curve) and comparison with Rosenbluth–Hinton theory (dotted curve). Analytic residual is shown as dotted horizontal line.

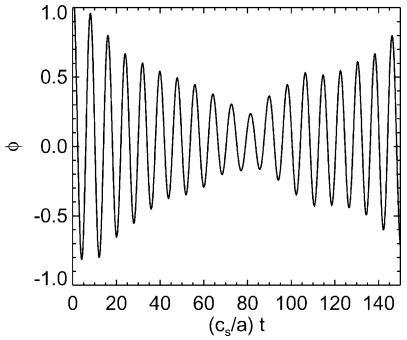

Fig. 10. Calculation of axisymmetric flow of previous figure, but without poloidal upwind dissipation. The collisionless damping effect is improperly treated.

respectively, with $v_1 = \sqrt{2T_1/m_1}$. The expression for ω_G which appears in Eq. (108) is more accurate than the estimate $\omega_G \sim v_1/R$ which appears in [38]. When combined with the formula for the residual potential, we expect a long-wavelength initial disturbance to behave as

$$\frac{\phi_k(t)}{\phi_k(0)} = (1 - A_R)e^{-\nu_G t}\cos(\omega_G t) + A_R, \quad \text{where } A_R = \frac{1}{1 + 1.6q^2/\sqrt{r_0/R}}. \tag{109}$$

Fig. 9 shows good agreement between the code and analytical results, even for the Landau damping rate. We remark that upwind differencing according to Eq. (30) is necessary to obtain this result. Attempting to use Eq. (29) for differencing of the axisymmetric GK equations leads to the erroneous result of Fig. 10. The physical interpretation is that upwind dissipation enforces causality by selecting the decaying mode. In an analytic solution of the Landau problem, one must analogously deform the integration contour to select the decaying mode of oscillations.

10.4. Nonlinear flux-tube benchmarks

A landmark paper which collected and compared results from preeminent ITG turbulence codes and models was authored by members of the Cyclone group [37]. The motivation for this work arose primarily from conflicting ITER [40] performance predictions supplied by these codes and models. Following the

comparison presented in that work, we scan χ_i versus R_0/L_T and compare with results from the LLNL and U. Colorado flux-tube PIC codes. The grid resolution used for all runs is summarized in case 1 of Table 6. The radial box was fixed at $\ell = 100\rho_s$ (this is equivalent to $24\ell_0$ with $k_\theta\rho_s = 0.3$, $s = 0.8$ and ℓ_0 as defined in Section 7).

Results of the parameter scan are shown in Fig. 11, indicating excellent agreement at lower driving rates, with some anomaly at higher driving rates – we hope to identify the cause of, and resolve, this difference shortly. Note that the onset of the "Dimits shift" [41] region (a region of almost zero transport despite the presence of unstable linear modes) at $R_0/L_T \simeq 6.0$ agrees well with the LLNL result. We remark that it is reported in [34] that the U. Colorado results (4 million particles) were not completely converged at this low value of R_0/L_T, while the LLNL results (8–34 million particles) were. As a consequence, we have omitted the U. Colorado results in the shift region. `gyro`, at 2.6 million gridpoints, is well converged in the shift region. The time-history of the `gyro` runs in the shift region appear in Fig. 12. After a steady level of transport out to $t = 400$, the $R_0/L_T = 6.0$ case drops to a low transport level coincident with the spontaneous excitation of long wavelength zonal flows. Fig. 12 also shows that the $R_0/L_T = 5.0$ case experiences a similar but more rapid decay to a final level $\chi_i/\chi_{GB} \leqslant 0.1$. Higher velocity-space resolution is required to approach $\chi_i = 0$ more closely: an $R_0/L_T = 5.0$ simulation with $n_\lambda = 12$ and $n_\epsilon = 12$ (not shown) gives $\chi_i/\chi_{GB} \leqslant 0.01$.

We have made a straightforward convergence study for the Cyclone DIII-D base case using the parameters shown in Table 6. The time histories of the diffusivities for the three tabulated cases are given in Fig. 13. The highest resolution run (case 1) gives the converged result previously plotted in Fig. 11. With resolution dropped to only 480,000 gridpoints, and timestep doubled to $\Delta t = 0.2$ (case 2), the `gyro` χ_i is only 1.3% less than the 2.6 million gridpoint case. With resolution dropped further to 173,000 gridpoints (case 3), we finally see a large discretization effect. At 480,000 gridpoints (case 2), the run time is slightly greater than 1 h on 32 processors of the NERSC IBM SP POWER3 machine. At 173,000 gridpoints (case

Table 6
`gyro` grid dimensions for Cyclone DIII-D base caseparameter scans of Figs. 11 and 12 (case 1) as well as for the convergence study shown in Fig. 6 (cases 1–3)

Case	n_r	n_τ	n_b	n_λ	n_ϵ	n_n	Δt
1	128	20	6	8	8	16	0.1
2	100	20	6	6	5	8	0.2
3	90	20	6	4	4	6	0.2

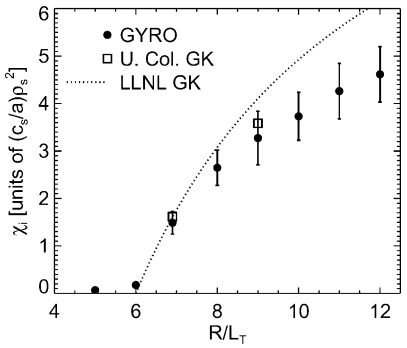

Fig. 11. χ_i versus R/L_T scan for the Cyclone DIII-D base case, compared with results from the LLNL and U. Colorado gyrokinetic PIC codes.

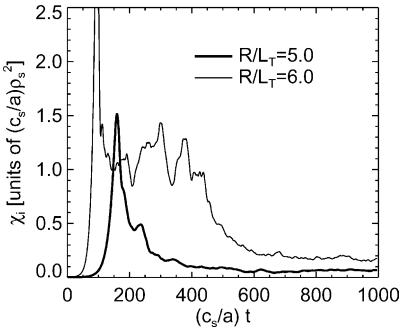

Fig. 12. Time-evolution of turbulent diffusivity for R_0/L_T in the Dimits shift region for the Cyclone DIII-D base case. Decay to almost zero diffusion is seen.

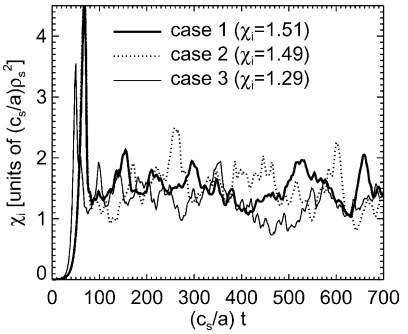

Fig. 13. Time-evolution of turbulent diffusivity for $R_0/L_T = 6.9$ showing converged result for less than 1/2 million gridpoints, and low but still sensible result for as few as 140,000 gridpoints. Numbers in parentheses are time-averaged diffusivities.

3), the run time is about 1.5 h on 32 processors of a 550 MHz Intel-beowulf cluster. Low-resolution PIC simulations behave differently, and for less than a half-million particles, flux-tube PIC codes tend to be noise-dominated at $(c_s/a)t > 200$ [41].

10.5. Nonlinear nonperiodic test case

We limit our discussion of nonperiodic boundary conditions to a test case which demonstrates their behavior with "flat profiles". If boundary effects are truly absent from the computational domain, we expect to measure the same diffusion from the flux-tube simulation as from the flat-profile nonperiodic simulation. Fig. 14 shows the results of such a comparison. The Waltz standard case parameters were used in a box of size $\ell = 80\rho_s$. This system is farther from marginal linear stability than the Cyclone DIII-D base case at $R_0/L_T = 6.9$.

Inside the computational domain (dotted line), the radial diffusivity profiles match quite well. With reference to Section 7, the dotted lines are $r = r_{Ld}, r_{Rd}$, the dashed lines are $r = r_{Lb}, r_{Rb}$ and the solid lines are $r = r_{Le}, r_{Re}$. These boundary conditions, when combined with an adaptive source, allow us to study systematically profile-related transport effects. Further discussion of nonperiodic ITG cases, profile shear stabilization, and broken gyroBohm scaling appears in [25].

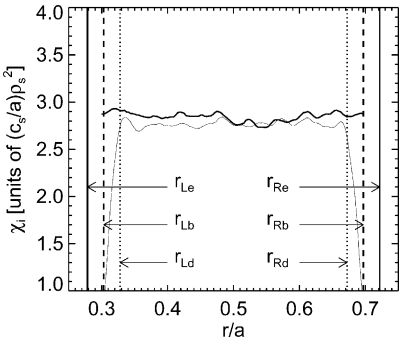

Fig. 14. Comparison of radial diffusivity profiles for flux-tube (thick curve) and nonperiodic (thin curve) code operation. Dotted lines are $r = r_{\mathrm{Ld}}, r_{\mathrm{Rd}}$, dashed lines are $r = r_{\mathrm{Lb}}, r_{\mathrm{Rb}}$ and solid lines are $r = r_{\mathrm{Le}}, r_{\mathrm{Re}}$.

11. Nonadiabatic electron benchmarks

Critical to the success of kinetic electron and finite-β_{e} simulations was exhaustive benchmarking with the `gks` code. In what follows we document a variety of linear cross-code comparisons.

11.1. Electron collisions

We will discuss only briefly the issue of collisions in the present work. The dominant collisional processes for typical parameters are electron–electron and electron–ion scattering. In the electrostatic limit, these give rise to diffusion of the electron distribution, h_2, in pitch-angle:

$$\mathscr{C}_2(h_2) = \frac{v_2(\epsilon)}{2}\frac{\partial}{\partial\xi}(1-\xi^2)\frac{\partial h_2}{\partial\xi}, \tag{110}$$

where $\xi \doteq v_{\parallel}/\sqrt{2\epsilon} \in [-1,1]$ is the cosine of the pitch-angle. Both electron–electron and electron–ion collisions are contained in v_{e}, which we write as

$$v_2(\epsilon) = \frac{v_{\mathrm{ei}}}{\epsilon^{3/2}}[Z_{\mathrm{eff}} + H_{\mathrm{ee}}(\sqrt{\epsilon})] \quad \text{with} \quad H_{\mathrm{ee}}(x) = \frac{e^{-x^2}}{\sqrt{\pi}x} + \left(1 - \frac{1}{2x^2}\right)\mathrm{erf}(x). \tag{111}$$

The electron–ion rate is $v_{\mathrm{ei}} \doteq \omega_{\mathrm{pe}}^2 e^2 m_{\mathrm{e}}^{1/2}\log\Lambda/(2T_{\mathrm{e}})^{3/2}$, with $\log\Lambda$ the Coulomb logarithm. Diffusion and slowing-down in energy are presently ignored. Momentum is not conserved by this collision operator; rather

$$\left(\frac{D}{Dt}\right)_{\mathrm{coll}}\int \mathrm{d}\xi\xi h_2 = -v_2(\epsilon)\int \mathrm{d}\xi\xi h_2. \tag{112}$$

Numerically, we run into some difficulty in treating pitch-angle scattering because h_2 is not known on an equally spaced θ-grid. Consequently, evaluation of the scattering operator $\mathscr{C}$ – which requires evaluation of $\partial/\partial\xi$ at constant θ – becomes a two-dimensional irregular grid problem. The diffusion term itself is split from the rest of the GK equation, and a partial time-advance of

$$\frac{\partial h_2}{\partial t} = \mathscr{C}_2(h_2), \tag{113}$$

is sought with an implicit scheme. The implicit scheme is necessary to overcome the extremely restrictive viscous Courant condition in the vicinity of the trapped-passing boundary (note the points close to the

trapped-passing boundary in Fig. 4). While the overall method is still experimental, it gives results which compare reasonably well with gks (Fig. 15). Nevertheless, much more work on collisional benchmarking is required. We will discuss the details of the (θ, ξ)-stencil selection algorithm, and generalization to electromagnetic fluctuations and energy diffusion, in a future publication.

11.2. β_e scans

Figs. 16 and 17 show growth rate and frequency comparisons, respectively, with the gks code for the Waltz standard case parameter set at $k_\theta \rho_s = 0.3$. Like all linear calculations in this paper, we use a periodic radial domain with $(n_r, n_d, n_g) = (6, 5, 6)$. The parameters $(n_\epsilon, n_\tau, n_\lambda)$ are the same as in Table 6 (case 1). The ideal MHD critical β_e for this case, which is slightly greater than 0.6%, is reflected in a jump from ITG to KBM branches. Below, at and above the critical β_e there is very good agreement with gks. There is a small discrepancy in the frequency of the KBM branch, very likely the result of inadequate grid resolution in one of the codes – as the KBM branch generally requires better energy resolution than the ITG branch. As an illustration of the quality of the solver, we give sample plots of electromagnetic eigenmodes as functions of the extended ballooning angle. The modes are not computed but reconstructed this way – using radial Fourier transforms – for diagnostic purposes. A representative low-β_e ITG mode is given in Figs. 18 and 19. Past the critical β_e, modes have the KBM polarization with nearly vanishing $E_\parallel$. Such modes are shown in

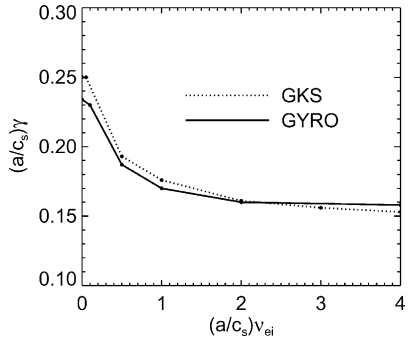

Fig. 15. Collision frequency scan comparing gyro (solid curve) and gks (dotted line) growth rates. The Waltz standard case parameters are used.

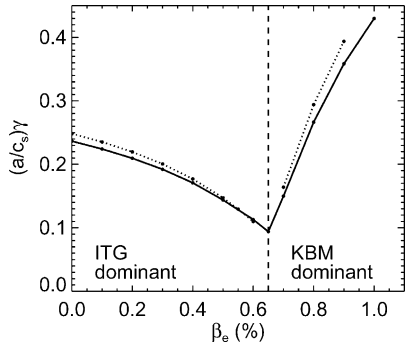

Fig. 16. β_e scan of growth rate for the Waltz standard case at $k_\theta \rho_s = 0.3$. gyro results are shown by solid curve, gks results by dotted curve.

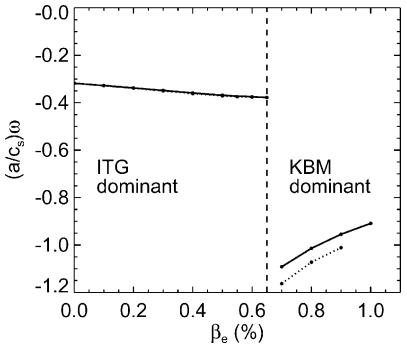

Fig. 17. Same as previous figure, except for frequency.

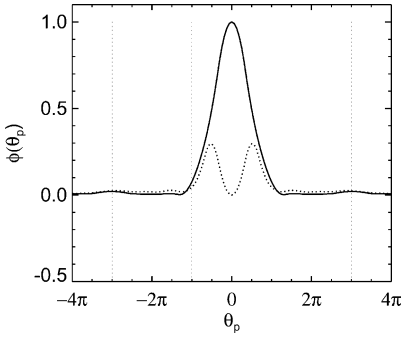

Fig. 18. Electrostatic potential, ϕ, as a function of ballooning angle for $\beta_e = 0.1\%$. Both the real (solid curve) and imaginary (dotted curve) parts are shown.

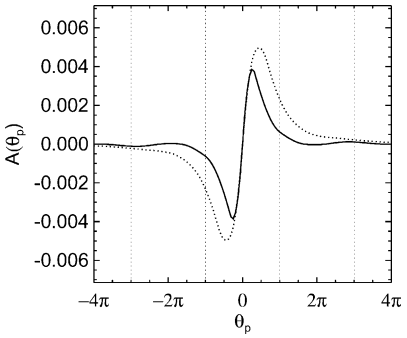

Fig. 19. Magnetic potential, $A_\parallel$, as a function of ballooning angle for $\beta_e = 0.1\%$. Both the real (solid curve) and imaginary (dotted curve) parts are shown.

Figs. 20 and 21. We remark that radial upwind differencing in the drift-advection terms is necessary when solving the electron equations on a ρ_i-scale grid. In cases where electron Landau layer effects do not need to be resolved, upwind dissipation eliminates unwanted numerical effects which would occur in a nondissipative scheme. The validity of the upwind approach relies on the constancy of the eigenvalue as the radial grid is refined.

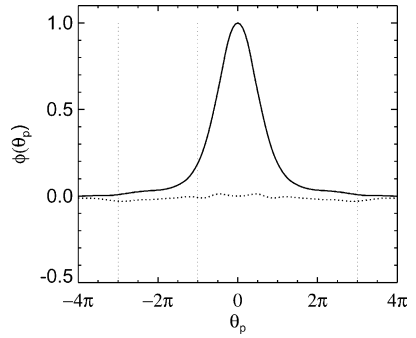

Fig. 20. Same as Fig. 18, but with $\beta_e = 1\%$.

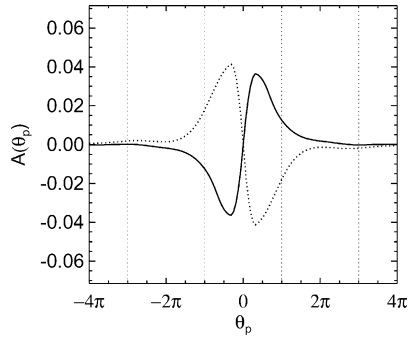

Fig. 21. Same as Fig. 19, but with $\beta_e = 1\%$.

Next, Figs. 22 and 23 show that decreasing the root of the mass ratio, $\mu = \sqrt{m_1/m_2}$, from 60 to 20 (with timestep given by $\mu\Delta t = 1.2$) results in a very minor perturbation to the growth rates and frequencies below the critical β_e. This observation motivated us to carry out nonlinear testing with the latter small value of the mass ratio with the benefit of reduced computational expense.

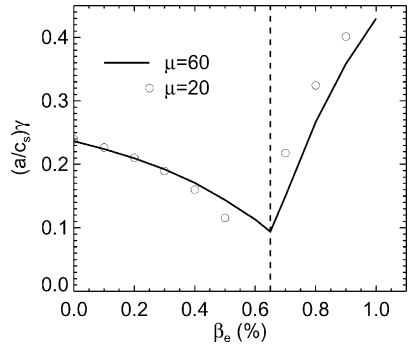

Fig. 22. Comparison of mode growth rates for real electrons with $\mu = 60$, and artificially heavy electrons with $\mu = 20$ for the Waltz standard case. The solid curve is taken from Fig. 16.

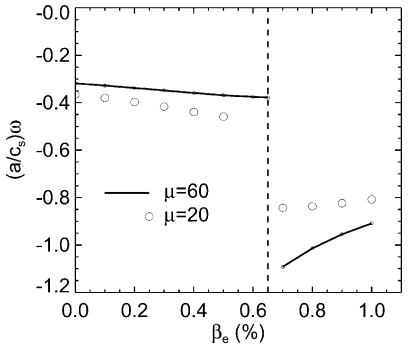

Fig. 23. Comparison of mode frequencies for real electrons with $\mu = 60$, and artificially heavy electrons with $\mu = 20$ for the Waltz standard case. The solid curve is taken from Fig. 17.

12. Electromagnetic transport calculations

Using the Cyclone DIII-D base case parameters with kinetic electrons and electromagnetic fluctuations, we performed preliminary nonlinear transport calculations for $\beta_e = [0.0\%, 0.25\%, 0.5\%]$. Grid resolution is summarized in Table 7, and the box size is $\ell = 100\rho_s$. We strongly caution the reader that the results are preliminary – in fact, we have indications that at the present grid resolution, results are not fully converged. The calculations are extremely expensive – each of the three simulations discussed in this section took roughly 44 h on 128 processors of the NERSC IBM SP RS/6000. Fig. 24 gives the ion and electron thermal diffusivities at $\beta_e = 0.0\%$. Figs. 25 and 26 give the same for $\beta_e = 0.25\%$ and $\beta_e = 0.5\%$ respectively. The ideal MHD critical β_e for this case is about 1.2%. Note that there is a small but measurable increase in transport. Much more work is needed to establish the physical validity of this effect. Attempts to simulate $\beta_e = 0.75\%$ have shown strongly intermittent results with extremely large excursions in diffusivity. The

Table 7
`gyro` grid for nonlinear electromagnetic cases

n_r	n_τ	n_b	n_λ	n_ϵ	n_n	Δt
128	20	6	8	5	16	0.02

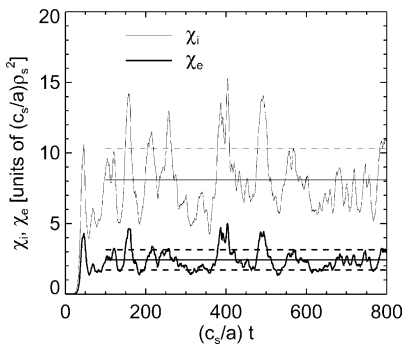

Fig. 24. Ion and electron thermal diffusivity (electrostatic components) at $\beta_e = 0.0\%$ for the Cyclone DIII-D base case. Trapped electrons are included. Here, $\bar{\chi}_i = 8.1 \pm 2.2$ and $\bar{\chi}_e = 2.4 \pm 0.7$. Particle diffusivities are $\bar{D}_i = \bar{D}_e = -1.0 \pm 0.3$.

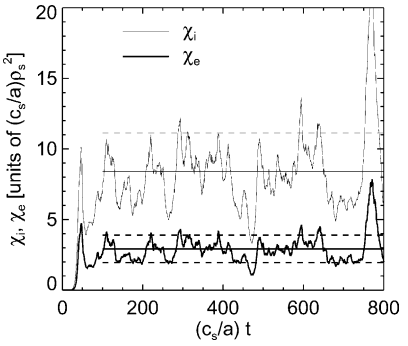

Fig. 25. Ion and electron thermal diffusivity (electrostatic components) at $\beta_e = 0.25\%$ for the Cyclone DIII-D base case. Trapped electrons are included. Here, $\bar{\chi}_i = 8.4 \pm 2.7$ and $\bar{\chi}_e = 2.9 \pm 1.0$. Particle diffusivities are $\bar{D}_i = \bar{D}_e = -0.1 \pm 0.4$.

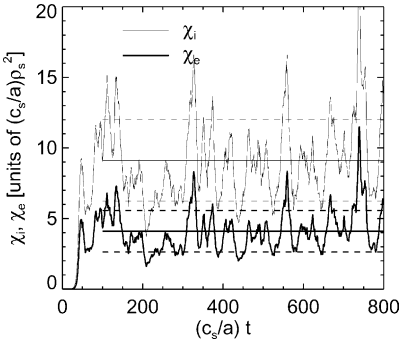

Fig. 26. Ion and electron thermal diffusivity (electrostatic components) at $\beta_e = 0.5\%$ for the Cyclone DIII-D base case. Trapped electrons are included. Here, $\bar{\chi}_i = 9.1 \pm 2.9$ and $\bar{\chi}_e = 4.1 \pm 1.5$. Particle diffusivities are $\bar{D}_i = \bar{D}_e = 1.8 \pm 1.2$.

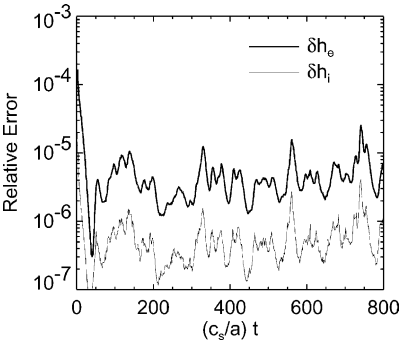

Fig. 27. Fractional time-integration error in the ion and electron distribution functions for $\beta_e = 0.5\%$. Not surprisingly, the electron error (δh_e, thick curve) is about 10 times greater than the ion error (δh_i, thin curve).

dynamical time-integration error for the $\beta_e = 0.5\%$ case is given in Fig. 27, indicating that this case was integrated forward with extremely high accuracy. To understand the effect of increasing β_e, it is instructive to look at plots of the time-averaged RMS intensity, $\langle \phi \rangle_{\mathrm{RMS}}$ in the $(k_r \rho_s, k_\theta \rho_s)$-plane. Fig. 28 shows the

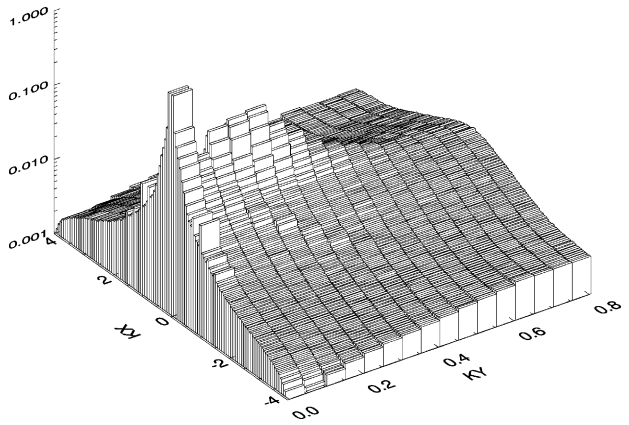

Fig. 28. Time-averaged RMS spectral density $\langle\phi\rangle_{\mathrm{RMS}}$ for $\beta_{\mathrm{e}} = 0.0\%$ as a function of $\mathrm{KX} \equiv k_r\rho_{\mathrm{s}}$ and $\mathrm{KY} \equiv k_\theta\rho_{\mathrm{s}}$.

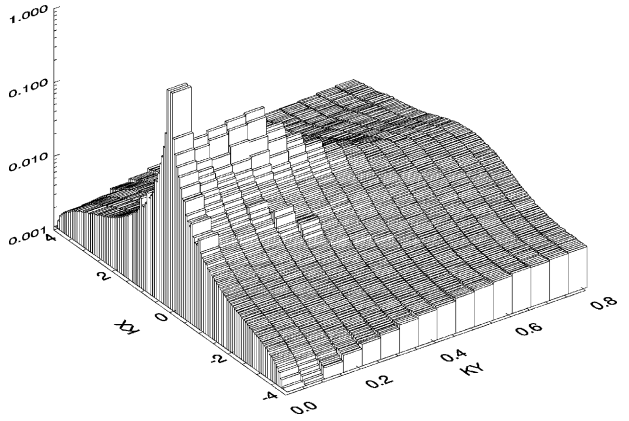

Fig. 29. Time-averaged RMS spectral density $\langle\phi\rangle_{\mathrm{RMS}}$ for $\beta_{\mathrm{e}} = 0.5\%$ as a function of $\mathrm{KX} \equiv k_r\rho_{\mathrm{s}}$ and $\mathrm{KY} \equiv k_\theta\rho_{\mathrm{s}}$.

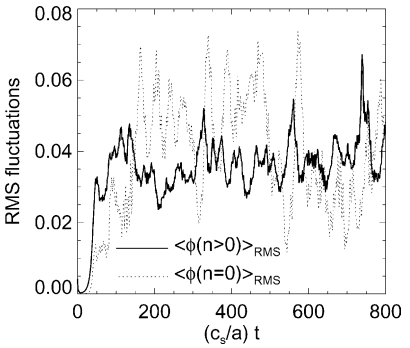

Fig. 30. Time-dependence of RMS intensities for axisymmetric (dotted curve) and nonaxisymmetric (solid curve) potentials for the Cyclone DIII-D base case at $\beta_{\mathrm{e}} = 0.5\%$.

spectrum for $\beta_e = 0.0\%$. When compared with the $\beta_e = 0.5\%$ in Fig. 29, we note a relative shift in intensity to lower values of k_θ.

Our experience with electrostatic simulations has shown that in the turbulent regime, and with adequate numerical resolution, the quantities $\langle \phi_{n=0} \rangle_{\mathrm{RMS}}$ and $\langle \phi_{n>0} \rangle_{\mathrm{RMS}}$ oscillate in time at about roughly the same mean value. This property tends to be strongly violated, with a run-away of one component, in the presence of a numerical instability. For the case $\beta_e = 0.5\%$, we find that the interplay between axisymmetric and nonaxisymmetric modes – as shown in Fig. 30 – gives no obvious indication of run-away.

13. Summary

The preliminary version of `gyro` was an attempt to extend the numerical methods used in `gks` and `gs2` beyond the limit of flux-tubes. We began with a semi-implicit time-advance algorithm in which linear terms were evolved implicitly (first-order temporal accuracy), and the nonlinear terms split and evolved separately using a fourth-order ERK method. This approach, which used a fixed poloidal grid, proved to have disastrous time-step convergence properties, even for ITG-ae simulations. Ironically, while the goal of the semi-implicit method was to circumvent the electron Courant condition $(v_{\|2}/qR)(\Delta t/\Delta\theta) < 1$, we found ourselves using values of Δt which satisfied this inequality even for adiabatic electron cases! This was the most fundamental lesson learned. Part of the reason for our difficulty was that the implicit scheme (really a specialized method for linear flux-tube calculations) was not easily generalized to the radial domain. Without flux-tube symmetry, a linear $\partial_r - \partial_\theta$ splitting was required for the GK equation, and distributed matrix operations (scaLAPACK) for the field-solve. The linear splitting caused zonal-flow instabilities which were overcome only with the use of an added predictor-corrector stage. Overall, the method was complex, expensive and inefficient. We were unable to reap the same apparent benefits as `gs2` in the use of implicit differencing.

These experiences were a clear indication that the problem required a completely different approach. Since the nonlinear terms, which can only be treated explicitly, set the timestep, it made no sense to us to pursue another semi-implicit discretization. Instead, we focused on explicit methods – keeping in mind always the most general form of the problem (kinetic electrons, finite-β, arbitrary profiles). The MOL approach was chosen because it provides a very general, flexible framework to explore different space and time discretizations without any a priori restrictions to a given discretization. We discovered quite soon that particle trapping posed a problem for all explicit methods (Section 4). This motivated the orbit-grid approach, which in turn necessitated the blending-function Maxwell solver. The speed and efficiency of the final algorithm makes ITG-ae transport calculations quite practical on even small Beowulf clusters (for example, the 46-processor GA cluster). We are confident that `gyro` will prove to be a valuable tool for the first-principles calculation of turbulent transport characteristics of current and next-step tokamaks.

Acknowledgements

This is a report of work supported by the US Department of Energy under Grant No. DE-FG03-95ER54309 and the Plasma Science Advanced Computing Initiative. We are deeply indebted to M.N. Rosenbluth for steady interest, criticism and advice during the developmental stages of this work. We also thank F.L. Hinton for algorithmic suggestions, as well as technical guidance on the topic of axisymmetric modes. To W. Dorland we express our gratitude for his help with benchmarking, for numerous helpful interactions, and for continued collaborative input. Finally, thanks to F. Jenko for discussions related to electromagnetic fluctuations.

References

[1] G. Rewoldt, W. Tang, M. Chance, Electromagentic kinetic toroidal eigenmodes for general magnetohydrodynamic equilibria, Phys. Fluids 25 (1982) 480.
[2] M. Kotschenreuther, G. Rewoldt, W. Tang, Comput. Phys. Commun. 88 (1995) 128.
[3] X. Garbet, R. Waltz, Action at distance and Bohm scaling of turbulence in tokamaks, Phys. Plasmas 3 (1996) 1898.
[4] R. Waltz, R. Dewar, X. Garbet, Theory and simulation of rotational shear stabilization of turbulence, Phys. Plasmas 5 (1998) 1784.
[5] G. Hammett, Plasma Phys. Control Fusion 35 (1993) 973.
[6] M. Beer, Gyrofluid models of turbulent transport in tokamaks, Ph.D. Thesis, Princeton University, 1995.
[7] R. Waltz, G. Kerbel, J. Milovich, Toroidal gyro-landau fluid model turbulence simulations in a nonlinear ballooning mode representation with radial modes, Phys. Plasmas 1 (1994) 2229.
[8] W. Dorland, in: Proc. 15th International Conference on Fusion Energy, vol. 3, Seville, Spain, 1994 (International Atomic Energy Agency, Vienna, 1995), p. 463.
[9] R. Waltz, G. Staebler, W. Dorland, G. Hammett, M. Kotschenreuther, J. Konings, Phys. Plasmas 4 (1997) 2482.
[10] M. Beer, G. Hammett, Phys. Plasmas 3 (1996) 4018.
[11] G. Hammett, in: Proc. 15th International Conference on Fusion Energy, vol. 3, Seville, Spain, 1994 (International Atomic Energy Agency, Vienna, 1995), p. 273.
[12] M. Beer, G. Hammett, G. Rewoldt, E. Synakowski, M. Zarnstorff, W. Dorland, Phys. Plasmas 4 (1997) 1792.
[13] R. Sydora, V. Becyk, J. Bawson, Fluctuation-induced heat transport results from a large global 3d toroidal particle simulation model, Plasma Phys. Control Fusion 38 (1996) A281.
[14] A. Bimits, Phys. Rev. Lett. 77 (1996) 71.
[15] S. Parker, C. Kim, Y. Chen, Large-scale gyrokinetic turbulence simulations: effects of profile variation, Phys. Plasmas 6 (1999) 1709.
[16] Z. Lin, T. Hahm, W. Lee, W. Tang, R. White, Gyrokinetic simulations in general geometry and applications to collisional damping of zonal flows, Phys. Plasmas 7 (2000) 1857.
[17] W. Dorland, F. Jenko, M. Kotschenreuther, B.N. Rogers, Phys. Rev. Lett. 85 (2000) 5579.
[18] F. Jenko, Massively parallel Vlasov simulation of electromagnetic drift-wave turbulence, Comput. Phys. Commun. 125 (2000) 196.
[19] W. Lee, Shear-alfv́en waves in gyrokinetic plasmas, Tech. Rep. PPPL-3495, Princeton Plasma Physics Laboratory, 2000.
[20] Z. Lin, L. Chen, A fluid-kinetic hybrid electron model for electromagnetic simulations, Phys. Plasmas 8 (2001) 1447.
[21] Y. Chen, S. Parker, A gyrokinetic ion zero electron inertia fluid electron model for turbulence simulations, Phys. Plasmas 8 (2001) 441.
[22] B. Cohen, A. Dimits, W. Nevins, Y. Chen, S. Parker, Kinetic electron closures for electromagnetic simulation of drift and shear-alfv́en waves (i), Phys. Plasmas 9 (2002) 251.
[23] B. Cohen, A. Dimits, W. Nevins, Y. Chen, S. Parker, Kinetic electron closures for electromagnetic simulation of drift and shear-alfv́en waves (ii), Phys. Plasmas 9 (2002) 1915.
[24] P. Snyder, G. Hammett, Electromagnetic effects on plasma microturbulence and transport, Phys. Plasmas 8 (2001) 744.
[25] R. Waltz, J. Candy, M. Rosenbluth, Gyrokinetic turbulence simulation of profile shear stabilization and broken gyroBohm scaling, Phys. Plasmas 9 (2002) 1938.
[26] R. Miller, M. Chu, J. Greene, Y. Lin-liu, R. Waltz, Noncircular, finite aspect ratio, local equilibrium model, Phys. Plasmas 5 (1998) 973.
[27] R. Waltz, R. Miller, Ion temperature gradient turbulence simulations and plasma flux surface shape, Phys. Plasmas 6 (1999) 4265.
[28] E. Frieman, L. Chen, Phys. Fluids 25 (1982) 502.
[29] A. Brizard, Nonlinear gyrokinetic Maxwell–Vlasov equations using magnetic coordinates, J. Plasma Phys. 41 (1989) 541.
[30] F. Jenko, W. Dorland, M. Kotschenreuther, B. Rogers, Electron temperature gradient driven turbulence, Phys. Plasmas 7 (2000) 1904.
[31] W. Dorland, G. Hammett, Phys. Fluids B 5 (1993) 812.
[32] D. Durran, Numerical Methods for Wave Equations in Geophysical Fluid Dynamics, Springer, New York, 1999.
[33] T. Davis, I. Duff, A combined unifrontal/multifrontal method for unsymmetric sparse matrices, ACM Trans. Math. Software 25 (1) (1999) 1–19.
[34] R. Burden, J. Faires, Numerical Analysis, Prindle, Weber and Schmidt, Boston, 1985.
[35] J. Connor, R. Hastie, J. Taylor, Proc. R. Soc. Lond. A 365 (1979) 1.
[36] C. Kennedy, M. Carpenter, R. Lewis, Low-storage, explicit Runge–Kutta schemes for the compressible Navier–Stokes equations, Tech. Rep. NASA/CR-1999-209349, ICASE, NASA Langley Research Center, 1999.
[37] A. Dimits, G. Bateman, M. Beer, B. Cohen, W. Dorland, G. Hammett, C. Kim, J. Kinsey, M. Kotschenreuther, A. Kritz, L. Lao, J. Mandrekas, W. Nevins, S. Parker, A. Redd, D. Shumaker, R. Sydora, J. Weiland, Comparisons and physics basis of tokamak transport models and turbulence simulations, Phys. Plasmas 7 (2000) 969.

[38] F. Hinton, M. Rosenbluth, Dynamics of axisymmetric $e \times b$ and poloidal flows in tokamaks, Plasma Phys. Control Fusion 41 (1999) A653.
[39] F. Hinton, private communication, 2001.
[40] R. Aymar, V. Chuyanov, M. Huguet, R. Parker, Y. Shimomura, in: Proc. 16th International Conference on Fusion Energy, vol. 1, Montréal, 1996 (International Atomic Energy Agency, Vienna, 1997), p. 3.
[41] A. Dimits, S. Parker, B. Cohen, C. Kim, N. Matter, W. Nevins, D. Shumaker, Simulation of ion temperature gradient turbulence in tokamaks, Nucl. Fusion 40 (2000) 661.